

Sub-nanometer 3D morphometric precision of polarisation-resolved wide-field optical extinction microscopy determines the roundness of individual gold nanospheres

Lukas M Payne,^{1,2} Furqan Alabdullah,^{3,2,4} Paola Borri,² and Wolfgang Langbein^{5,6}

¹*School of Physics and Astronomy, Cardiff University, The Parade, Cardiff CF24 3AA, United Kingdom*

²*School of Biosciences, Cardiff University, Museum Avenue, Cardiff CF10 3AX, United Kingdom*

³*School of Engineering, Cardiff University, The Parade, Cardiff CF24 3AA, United Kingdom*

⁴*Engineering Technical College of Al-Najaf, Al-Furat Al-Awsat Technical University, Najaf 31001, Iraq*

⁵*Cardiff University School of Physics and Astronomy, The Parade, Cardiff CF24 3AA, United Kingdom*

⁶*Corresponding author, langbeinww@cardiff.ac.uk*

(Dated: 10 February 2026)

Quantitative polarisation-resolved optical extinction microscopy of individual plasmonic nanoparticles has recently been introduced as a powerful tool to characterise the nanoparticle's morphology with a precision comparable to electron microscopy, while using a simple optical microscope [Nanoscale 12, 16215 (2020)]. Here we provide a step change by adding measurements for radial polarisation in the condenser back focal plane, probing plasmonic resonances polarised in axial direction. The combined linear and radial polarisation measurements provide a significantly enhanced precision of the retrieved 3D morphology, as we show on defect-free ultra-uniform gold nanospheres of 30 nm nominal diameter characterised by transmission electron microscopy. The measured cross-sections are modelled for an ellipsoidal particle, determining the three semi-axes and rotation angles by fitting the measurements. The material permittivity and surface damping providing the best fit are found. The particle aspect ratio is determined with a precision better than 5%, and the size with an impressive precision of 0.1 nm. Notably, corrections to the Rayleigh-Gans ellipsoid model due to retardation are significant even though the particle diameters are more than an order of magnitude smaller than the wavelength in the medium. Taking them into account improves the shape accuracy.

I. INTRODUCTION

Over the last decades, nanoparticles (NPs) and nanostructured materials have become increasingly important in many fields, from biological and medical imaging,^{1,2} to sensing,^{3,4} catalysis,^{5,6} and drug-delivery.^{7,8} Considering the plethora of nano-objects produced by human activity, studies of NP wastes and environmental contaminations⁹ have attracted increasing attention. Throughout these spaces, the size and shape of NPs play key roles, hence their accurate characterization is important.¹⁰

For NPs larger than the diffraction limit of visible light of around 250 nm, optical microscopy can directly resolve NP morphology. However, for smaller NPs such a characterization remains a significant challenge. To date, the industry standard for NP morphometry remains transmission electron microscopy (TEM),^{10,11} but due to high capital and operating costs, TEM is often not economically viable. Additionally, TEM is time-consuming, specifically if tomography is needed for 3D analysis, limiting the number of NPs measured and thus the statistical relevance of the results. Furthermore, the high energy electron beam used can lead to NP damage/reshaping during measurements. These aspects hinder the applicability of TEM to provide high-throughput and reliable statistical assessment of samples, a critical feature to quality control in NP manufacturing.

Apart from microscopy, in recent years techniques exploiting NP mechanical properties have shown promise in NP sizing, such as centrifugation,^{12,13} field-flow fractionation

(FFF) in various implementations,^{13–15} and tunable resistive pulse sensing (TRPS),^{13,16,17} Various versions are commercially available as benchtop devices, but these techniques also exhibit limitations. Centrifugation methods yield ensemble properties of particles only, and all methods provide size but not shape metrics, except FFF which provides indirect shape information.

Popular optical methods for NP morphometry use the light scattered from an incident field by NPs in suspension, to monitor their motion in a viscous liquid medium. These methods include dynamic light scattering (DLS),¹⁸ nanoparticle tracking analysis (NTA),^{19,20} and interferometric NTA (iNTA).²¹ Both DLS and NTA are implemented in commercially available benchtop devices, with DLS being an industrial standard for rapid sample size characterization. DLS is an ensemble measurement technique, strongly affected by sample polydispersity, while NTA and iNTA both provide single particle measurements, overcoming this issue. However, all three assume a spherical particle shape undergoing Brownian motion to determine the hydrodynamic radius, which is in itself distinct from the physical radius. Hence, these methods provide no shape information, and use the optical measurements only indirectly to determine the NP size. A nanofluidic scattering-based technique also exists, but is presently restricted to determining the hydrodynamic radius as well.²² Alternatively, depolarised dynamic light scattering (DDLS) leverages detection of the co- and cross-polarised components of the scattering signal to measure the translational and rotational diffusion coefficients, and subsequently the length and diameter of

the particles assuming a rod or cylindrical-like particle model. However, being a DLS-based technique, it still lacks individual particle measurements, and the determined values are reflective of the apparent size from the NPs motion through liquid. Other recent advances in photopolarimetric techniques without²³ and with²⁴ structured illumination exhibit similar limitations. Additional methods include through-focus scanning optical microscopy (TSOM)²⁵ and through-focus interferometric nanoparticle imaging^{26,27} which use the measured signal from particles at different focus positions.

Complementary approaches directly measure optical properties for diffraction-limited NP morphometry, using either the complex polarisability,^{28,29} or the optical cross-sections, namely absorption σ_{abs} ,^{30–32} scattering σ_{sca} ,^{33–35} and extinction σ_{ext} .^{31,34,36,37} σ_{abs} and σ_{sca} are fundamentally related to the NP polarisability, and quantify the ability of an object to absorb or scatter light, respectively. The extinction cross-section, σ_{ext} , is the sum of the absorption and scattering, and is given by the effective area blocked by the particle for a collimated incident field. The polarisability and the cross-sections of NPs of given size and shape can be calculated by analytical models only in special cases, such as spheres,³⁸ or ellipsoids within the dipole approximation,³⁹ while for more complex shapes numerical models are needed.^{40–42} These optical methods may be employed in conjunction with a physical model, to compare theoretical predictions of morphometry-dependent optical properties with optical measurements, and then infer the NP size and shape, frequently referred to as ‘solving the inverse problem’.

Recently, our group established a methodology for 3D morphometry of single NPs called the Optical Nanosizer (ON).⁴³ As a wide-field microscopy modality, the ON offers simultaneous measurement of up to hundreds of NPs in a single field of view, with a sensitivity down to $\sigma_{\text{ext}} \approx 1 \text{ nm}^2$, similar to the cross-section of a gold nanosphere (GNS) of $D \approx 2 \text{ nm}$ diameter. In this method, a series of brightfield transmission images of NPs deposited on a coverslip are captured on a conventional microscope under illumination at different wavelengths and linear polarisations. Dark-field images can be additionally taken to distinguish scattering and absorption cross-sections.³⁵ Images are analysed as differential transmission contrast, to quantify σ_{ext} for each NP in the field of view. By comparing the Rayleigh–Gans model for ellipsoidal particles with the measurements of σ_{ext} for each NP in the images, we inferred the size and shape of nominally spherical small (10 to 30 nm diameter) gold nanoparticles, and gold nanorods (10 nm diameter, 30 nm length). The precision of the method was found to be $\pm 0.5 \text{ nm}$ for size, and about 10% for the shape anisotropy. In terms of accuracy, we found the measurements of GNS having nominal diameter, $D = 30 \text{ nm}$, to be within 1 nm of TEM characterization on the same sample, i.e. showing only about 4% discrepancy. Notably, for shape retrieval we used linearly polarised excitation light in the condenser back focal plane with varying in-plane angle. Even with a high numerical aperture (NA) condenser focussing the light, only a small fraction of light at the sample is polarised out of plane, i.e. axially. Hence, the measurements are dominated by excitation polarisations in the sample plane, and thus are

more sensitive to the in-plane geometry of the NP. The out-of-plane geometry was therefore indirectly retrieved by spectral properties using the dependence of surface plasmon resonance frequencies on particle morphology.

In this work, we present an ON with 3D shape recovery independent of orientation, by using both linear and radially polarised illumination. In conjunction with a high NA condenser, radially polarised light creates a strong axial polarisation component at the sample. This provides a direct probe of the out-of-plane NP geometry, while the linear in-plane polarised illumination probes the in-plane NP geometry. We examine nominally $D = 30 \text{ nm}$ ‘ultra-uniform’ gold nanospheres (UGNS) to demonstrate the ON capabilities. Notably, these UGNS had been characterized with high-angle annular dark-field scanning transmission electron microscopy (HAADF-STEM) in our previous works,^{43,44} including tomography on selected cases, providing a reliable morphometry ground truth. The new ON method shows a significant improvement in precision and accuracy of 3D size and shape retrieval, reaching impressive sub-nm values.

II. MODEL: PERMITTIVITY, POLARISABILITY, AND OPTICAL CROSS-SECTIONS

The previous ON analytical developments were described in detail in Ref. 43 and 44. We build here on this analysis, extending it to add the treatment of the radially polarised illumination. We briefly recap the model in the following. The morphometry of each particle is derived from the measured cross-sections by solving ‘the inverse problem,’ using a theoretical framework relating the geometry of a NP to its optical cross-sections. Modelling the optical cross-sections requires knowledge of the complex permittivity of the NP material. In the literature, different measured spectra of the permittivity of gold are provided. We considered three of these, namely the data of Johnson & Christy (JC),⁴⁵ McPeak et al. (MP),⁴⁶ and Olmon et al. (OL).⁴⁷ They were measured by spectroscopic ellipsometry on thin polycrystalline films (JC, MP) or single crystalline gold (OL). To account for a surface damping effect in the NPs, we use the following approach. The permittivity is described by a Drude model with a bound electron contribution stemming from the interband transitions from the d bands into the conduction band, and surface damping effects, given by,^{35,48}

$$\epsilon_{\text{NP}} = 1 - \frac{\omega_p^2}{\omega(\omega + i\Gamma)} + \epsilon^b(\omega), \quad (1)$$

with ω_p the plasma frequency, ϵ^b the bound electron contribution^{48,49}, and Γ the Drude damping rate. A surface damping term is included in Γ , which is approximated⁵⁰ by

$$\Gamma = \Gamma_0 + g \frac{v_F}{R}, \quad (2)$$

with the NP radius, $R = D/2$, the bulk damping rate, Γ_0 , the Fermi velocity in gold,⁵¹ $v_F = 1.4 \times 10^6 \text{ m/s}$, and a dimensionless number, g , parameterizing the surface damping – Table

S.1 of Ref. 35 provides the complete parameterization including $\epsilon^b(\omega)$. Assuming $g = 0$, we determine the values of all the other parameters by using Eq. 1 to independently fit each experimental gold permittivity dataset. Using these parameters, we determine a series of ϵ_{NP} evaluated with different values of $g \in [0, 4.5]$, covering the range of g reported in the literature.^{37,48}

We use the Rayleigh–Gans model, describing ellipsoidal NPs much smaller than the light wavelength (λ), to determine the NP polarisability using the complex material permittivity and geometry of the NP, and the permittivity, ϵ_m , of the surrounding medium. As introduced in Ref. 44, we use a Cartesian reference system of unit vectors \vec{e}'_κ , with $\kappa = x', y',$ and z' which respectively point in the directions of the three semi-axes of an ellipsoidal NP of length (a, b, c) , which we order such that $a \geq b \geq c$. In this basis, the polarisability tensor α' is a diagonal matrix. The diagonal elements are the polarisabilities for fields oriented along each of the NP's semi-axes, given by

$$\alpha'_j = V\epsilon_0 \frac{\epsilon_{\text{NP}} - \epsilon_m}{\epsilon_m + L_j(\epsilon_{\text{NP}} - \epsilon_m)}, \quad (3)$$

where V is the NP volume, ϵ_0 is the free space permittivity, ϵ_m is the dielectric function of the surrounding medium, and L_j are depolarisation factors, with $j \in \{1, 2, 3\}$. The geometry of the NP determines L_j . For example, for a sphere, $L_j = 1/3$. ϵ_m is assumed to be real and frequency independent. All materials are assumed to be non-magnetic, i.e. with relative permeability $\mu_r = 1$. We note that metals exhibit a zero crossing versus wavelength of the real part of the denominator in Eq. 3 at $\Re\{\epsilon_{\text{NP}}\} = (1 - L_j^{-1})\epsilon_m$, which results in a peak in σ_{ext} called the localised surface plasmon resonance (LSPR). For an incident field \vec{E}' , the induced electric dipole moment is given by

$$\vec{p}' = \alpha' \vec{E}'. \quad (4)$$

We choose a Cartesian coordinate system to describe the laboratory frame, with axes $\iota \in \{x, y, z\}$, and associated unit vectors \vec{e}_ι , where \vec{e}_z points along the optical path, and \vec{e}_x, \vec{e}_y span the sample plane. To transform α' into the laboratory reference frame, we define⁴³ a 3D rotation matrix using $R = R_\psi R_\theta R_\phi$ and $R^\top = R_\phi^\top R_\theta^\top R_\psi^\top$, with ϕ, θ, ψ the angles of rotation about $\vec{e}_x, \vec{e}_y, \vec{e}_z$, respectively. We transform a vector from the NP frame into the laboratory frame with $\vec{v} = R\vec{v}'$. Eq. 4 becomes $R^\top \vec{p} = \alpha' R^\top \vec{E}$, such that the polarisability in the laboratory frame is given by

$$\alpha = R\alpha'R^\top. \quad (5)$$

The scattering and absorption cross-sections, σ_{sca} and σ_{abs} are the power scattered (P_{sca}) or absorbed (P_{abs}) from the incident field by the NP relative to the intensity, I_{inc} , of the incident field, $\sigma_{\text{sca}} = P_{\text{sca}}/I_{\text{inc}}$ and $\sigma_{\text{abs}} = P_{\text{abs}}/I_{\text{inc}}$. Within the dipole approximation $D \ll \lambda$ the optical cross-sections are given by

$$\sigma_{\text{abs}}(\vec{E}) = \frac{k}{\epsilon_0} \frac{\Im(\vec{E}^* \cdot \vec{p})}{|\vec{E}|^2}, \quad (6)$$

and

$$\sigma_{\text{sca}}(\vec{E}) = \frac{k^4}{6\pi\epsilon_0^2} \frac{|\vec{p}|^2}{|\vec{E}|^2}, \quad (7)$$

with $(*)$ indicating complex conjugation, and $k = 2\pi n_m/\lambda$, the wavenumber in the medium of refractive index $n_m = \sqrt{\epsilon_m}$.

To compare the ellipsoid geometry with plan-view TEM characterisation, we define a mean aspect ratio (MAR), \sqrt{bc}/a , and a projected aspect ratio (PAR) given by b'/a' , with the semi-axes lengths a' and b' in the xy -plane of the ellipsoid projected along the z axis (for calculation details see Sec. B). We also define the corresponding projected diameter as $D_p = 2\sqrt{a'b'}$ and a volume-equivalent diameter as $D_V = 2\sqrt[3]{abc}$.

III. EXPERIMENT

A detailed description of the microscope setup and data analysis are provided in Ref. 43. A brief overview of the setup and samples used in this work is given in the following.

A. Optical Measurements

We performed wide-field optical transmission measurements on a Nikon Ti-U inverted microscope, with illumination provided by a 100 W tungsten halogen lamp, using bandpass filters of 40 nm width and center wavelengths $\Lambda \in \{450 \text{ nm}, 500 \text{ nm}, 550 \text{ nm}, 600 \text{ nm}, 650 \text{ nm}, 700 \text{ nm}\}$. A 1.34 NA oil-immersion condenser (Nikon MEL41410) focused the illumination to the sample. The transmitted light was collected by a 1.45 NA 100 \times oil immersion objective (Nikon MRD01905) and imaged by a 1.0 \times tube-lens onto the camera with a magnification of $M = 100$. A motorised linear polariser in the collimated light path towards the condenser controlled the excitation polarisation angle γ_p , and a motorised slider switched between linear and radial polariser.⁵² A scientific-CMOS (sCMOS) camera (PCO Edge 5.5) at the eyepiece port was used for image acquisition, having 2560×2160 pixels with a full-well capacity of $N_{\text{fw}} = 30000$ electrons. Illumination intensities and exposure times were chosen to result in pixel values around 50000 counts of the 16-bit digitizer range, which for the gain of 0.54 electrons/count corresponds to about 27000 electrons, close to N_{fw} without entering a non-linear response range. For each wavelength, taken in ascending order, the sample was focussed, and then data were taken for linear polarisation at γ_p of 0, 45, 90 and 135 degrees, and radial polarisation. A sketch of the microscope set-up and sample geometry is shown in Fig. 1, and more details are given in Ref. 52.

B. Samples

'Ultra-uniform' gold NPs of nominal spherical shape and mean diameter, $D = 30 \text{ nm}$, were obtained from NanoComposix. To observe small gold NPs with extinction microscopy,

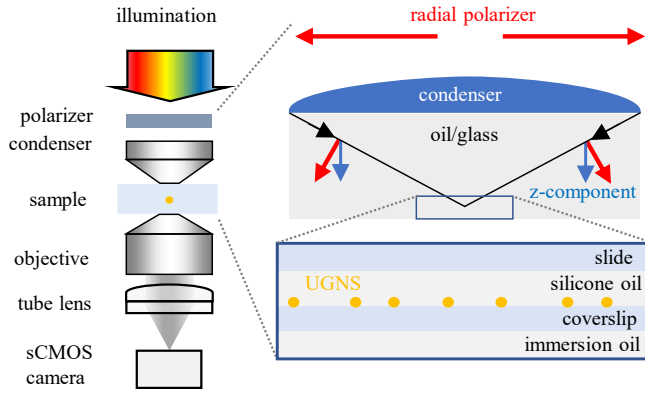


FIG. 1. Sketch of the microscope set-up and investigated sample. Under Köhler illumination of selectable wavelength range, the sample is imaged onto a camera, using a 1.34 NA condenser and a 1.45 NA objective. In the illumination a rotatable linear polariser or a radial polariser are used, the latter generating a significant axially-polarised illumination component in the focal plane. The sample consists of individual gold nanospheres deposited onto a glass coverslip, surrounded by silicone oil index-matched to glass.

glass slides and coverslips (Menzel-Gläser, #1.5) have to be optically clear, with no contamination or debris. This was achieved using a cleaning process involving sonication steps in toluene, acetone, a water rinse followed by treatment with boiling deionised (DI) water, and then storage in 30% hydrogen peroxide for at least one day before preparation. A wet casting method was used for NP deposition, to prevent surface tension-induced aggregation during the sedimentation of NPs on the coverslips in a dry environment. The concentration of NPs in the suspension applied onto the glass surface was adjusted to achieve a surface density with individual NPs separated by a few microns. The stock concentration provided by the manufacturer was diluted accordingly. Slides and coverslips were rinsed with DI water, dried in a nitrogen flow, and 50 μL of the diluted NP suspension was evenly spread across the whole coverslip surface. The sample was placed in a 100% humidity environment for one hour, to allow NP sedimentation via wet casting. Afterwards, the coverslip was gently rinsed with DI water, positioned vertically to allow excess water to drain, and dried in a nitrogen flow. Then, 25 μL of silicone oil (AP150, Wacker), index-matched to glass, was pipetted onto the coverslip to create an index-matched medium surrounding the NPs. A glass slide was placed over the oil-covered surface, and the coverslip was pressed manually to reduce the oil layer thickness. Excess oil at the edges of the coverslip was removed and the sample was sealed by applying nail varnish to the edges of the coverslip.

C. Optical Extinction Measurements

In Ref. 53 we detailed our procedure to quantitatively measure σ_{ext} , with additional information given in Ref. 54. In short, two *brightfield* images called I_1 and I_2 are captured,

which differ only by a lateral shift of the sample, typically 1 to 2 μm (i.e. a few optical resolutions). I_1 and I_2 are averaged in real time over a number, N_i , of individual acquisitions to reduce shot noise. We compute $\Delta_{1,2} = 1 - I_{1,2}/I_{2,1}$ to yield two extinction images (with inverted contrast). To further reduce shot noise as well as systematic noise due to sensor electronic drift, we can average the extinction over a number of repetitions N_r . For a NP centered in the areas $A_{1,2}$ of radius r_i in $I_{1,2}$, we determine its extinction as $2\sigma_{\text{ext}} = \int_{A_1} \Delta_1 dA + \int_{A_2} \Delta_2 dA$. We calculate the shot-noise-limited standard deviation in the measured σ_{ext} as⁵³

$$\hat{\sigma}_{\text{ext}} = \frac{r_i d_{\text{px}}}{M} \sqrt{\frac{\pi}{N_a N_{\text{fw}}}}, \quad (8)$$

where M is the magnification from the sample to the detector, $N_a = N_i N_r$ is the number of acquired frames, and $d_{\text{px}} = 6.5 \mu\text{m}$ is the pixel pitch of the sensor. We previously used³⁴ a measurement radius of $r_i = 3\lambda/(2\text{NA})$ to analyse σ_{ext} , and the effect of r_i on σ_{ext} is characterised in detail in Ref. 55. In the present work, we employ three values of r_i , specifically $r_s = 3\lambda/(2\text{NA})$, $r_h = 1.2r_s$, and $r_l = 0.8r_s$, with $N_i = 128$ and $N_r = 20$. At $\Lambda = 550\text{nm}$, Eq. 8 yields $\hat{\sigma}_{\text{ext}} \approx 7.5\text{nm}^2$ using r_s , while the noise seen in the extinction data at this wavelength is 15.6nm^2 . The additional noise is attributed to surface roughness, debris, and/or residual sensor fluctuations, as analysed in detail in Ref. 53. We note that measurements are taken over several different fields of view (FOV) and aggregated for the final statistics. The $\hat{\sigma}_{\text{ext}}$ reported are the polarisation-averaged values of the noise, averaged over the measured values from all the FOVs. We found that $\hat{\sigma}_{\text{ext}}$ varies by $\pm 5\%$ across the illumination polarisations, and by $\pm 15\%$ across FOVs. We measure σ_{ext} for multiple wavelengths Λ , both for the linear polariser at multiple angles γ_p , denoted as $\sigma_{\Lambda}(\gamma_p)$, and for the radial polariser, denoted as $\sigma_{\Lambda}(\gamma_R)$. The noise $\hat{\sigma}_{\text{ext}}$ refers, in general, to the value specific to the data of each Λ , polarisation, and field-of-view (see Sec. III A for Λ and γ_p values used). The wavelength dependence of the noise is shown in the inset of Fig. 2a.

We model the polarisation dependence of σ_{ext} for linear polarisation as

$$\sigma(\gamma_p) = \sigma \{1 + \alpha \cos[2(\gamma_p - \gamma)]\}, \quad (9)$$

where σ is the average cross-section, and the polarisation dependence is given by a relative amplitude $\alpha \in [0, 1]$, which encodes the dipolar in-plane asymmetry of the NP, with $\alpha = 0$ indicating the absence of such asymmetry. The maximum of $\sigma(\gamma_p)$ is at the angle $\gamma \in [0, \pi]$, providing the orientation of the asymmetry in the sample plane.

The finite bandwidth of the filters used means the measured σ_{Λ} are averaged over the respective wavelength ranges. Additionally, while the transmission of the filters is approximately flat over their ranges, the illumination intensity and camera sensitivity are not. To take these features into account in our model of σ_{ext} , we compute weighted averages over each Λ for each polariser angle, as

$$\sigma_{\Lambda} = \frac{\int_{\Lambda} w(\lambda) [\sigma_{\text{abs}}(\lambda) + \sigma_{\text{sca}}(\lambda)] d\lambda}{\int_{\Lambda} w(\lambda) d\lambda}, \quad (10)$$

where $w(\lambda) = l(\lambda)c(\lambda)$ is the weighting incorporating the normalized illumination spectral intensity, $l(\lambda)$, and camera sensitivity, $c(\lambda)$, as functions of wavelength λ . The lamp spectrum is modeled as a blackbody radiator at temperature, $T = 2800\text{K}$, as described in Section 2.1.4 of Ref. 54. The camera sensitivity is known from the manufacturer and was digitized for this work. The wavelength dependence of $w(\lambda)$ is shown in Fig. 6.

IV. RESULTS AND DISCUSSION

This work demonstrates the enhanced capabilities of the new ON including radial polarisation in determining individual NP morphometries in 3D. We maintain the naming and definitions of variables and quantities used in our previous publications,^{43,44} and introduce them in the text where needed. All analysis assumes that the refractive index of the NP environment in the samples is $n_m = 1.52$. The effect of variation of this index is discussed in Sec. F.

A. Statistical Distributions of σ_Λ and α_Λ

We first introduce relevant quantities used in the statistical description of the optical measurements. For each NP, Eq. 9 is fitted to the $\sigma_\Lambda(\gamma_p)$ measured for linear polarisation, determining its parameters σ , α , and γ . Their standard errors $\hat{\sigma}$, $\hat{\alpha}$, and $\hat{\gamma}$ are determined using a Monte Carlo simulation where we add random Gaussian noise to the measured data, matching the experimentally determined noise, as detailed in Ref. 43 and Sec. C.

Given a set of N NPs, numbered by the index, i , we identify the fit parameters using the subscript Λ, i , and define the sample-wide mean of $\sigma_{\Lambda, i}$ to be $\bar{\sigma}_\Lambda = \frac{1}{N} \sum_{i=1}^N \sigma_{\Lambda, i}$, and the associated standard deviation $\hat{\sigma}_{\Lambda, m}$. Equivalent quantities are defined for the other two parameters. Correcting for the measurement noise, the standard deviation $\hat{\sigma}_\Lambda = \sqrt{\hat{\sigma}_{\Lambda, m}^2 - \frac{1}{N} \sum_{i=1}^N \hat{\sigma}_{\Lambda, i}^2}$ represents the distribution of NP cross-sections originating from their sizes and shapes only. For the relative amplitude parameter, the measurement error $\hat{\alpha}_{\Lambda, i}$ varies strongly depending on the parameter values, so that we refrain from such a correction and directly use $\hat{\alpha}_\Lambda = \hat{\alpha}_{\Lambda, m}$.

The UGNS are highly uniform in size and shape as previously measured by HAADF-STEM.⁴⁴ Specifically, we considered the projected diameter D_p and the PAR using the shorter, b' , to longer, a' , semi-axes observed in plan-view STEM, and found distributions characterised by mean and standard deviation values of $(\bar{D}_p \pm \hat{D}_p) = (28.04 \pm 1.54)$ nm for the diameter and 0.977 ± 0.024 for the PAR. The median $M\{\cdot\}$ over the N NPs analyzed is found to be $M\{D_p\} = 27.75$ nm and $M\{\text{PAR}\} = 0.985$. From this prior knowledge, we can expect for our optical measurements: (1) a narrow distribution of both σ_Λ and α_Λ , (2) a small in-plane asymmetry $\bar{\alpha}_\Lambda \ll 1$ for all Λ where $\bar{\sigma}_\Lambda \gg \hat{\sigma}_{\text{ext}}$, (3) $\bar{\sigma}_\Lambda$ to be close to the theoretically predicted value for a GNS of the expected size.

Fig. 2 presents σ_Λ and α_Λ for measurements of the $N = 51$

nominally $D = 30\text{nm}$ UGNS for all Λ of the experiment. To mitigate small differences in focus between the different fields of view, σ_{ext} was determined using the larger radius r_h (see Sec. D for more details). One must correct σ_{ext} obtained with a finite r_i to compensate for the signal outside of the integration area. The correction factor to σ_{ext} was determined to be $c_1 = 1.12$, $c_s = 1.06$, and $c_h = 1.02$, for r_1 , r_s , and r_h , respectively. In Fig. 2 we show σ_{ext} as measured and the modelled extinction divided by c_h . Narrow distributions of σ_Λ are observed for all Λ . Small in-plane asymmetries $\alpha_\Lambda < 0.2$ are found for about 95% of the NPs at $\Lambda = 600$ and below, and for about 80% of NPs at $\Lambda = 650$. At $\Lambda = 700$ instead, σ_{ext} is only a few times larger than the noise, which results in a wide distribution of α_Λ estimated by the shaded areas. Hence, the sample exhibits a low optical asymmetry, with some 10% outliers.

Looking at the simulations in the inset of Fig. 2, we note that $\Lambda = 550$ covers the higher wavelength side of the LSPR of a spherical gold NP, suggesting that accurately modelling the width of the channels will be relevant for the morphology retrieval. With increasing NP asymmetry, the LSPR polarised along the longer axis (the longitudinal mode) red-shifts, increasing its overlap with the 550 channel, and thus providing a sensitive probe of asymmetries. We find $\bar{\alpha}_{550} = 0.037 \pm 0.039$, with some 80% of NPs showing $\alpha_{550} < 0.054$, and the rest clearly asymmetric with α_{550} up to 0.194. For asymmetric NPs, the LSPR will move into the increasingly red channels (see simulations in Ref. 43 Fig. 2), increasing their σ_Λ and α_Λ . Looking at the exemplary TEM image, some 10-20% of significantly non-spherical NPs can be expected. Their red-shift can be significant, contributing to the values of α_{650} and α_{700} well above the noise. We also note that the $\Lambda = \{450, 500\}$ channels are rather insensitive to asymmetry, due to the dominant absorptive part of the permittivity, $\Im\{\epsilon_{\text{NP}}\} \approx 5$, with $\Re\{\epsilon_{\text{NP}}\}$ similar to ϵ_m , suppressing shape-dependent effects, so that σ_{450} and σ_{500} are good reporters of the NP volume.

Let us now discuss σ_{ext} measured using the radial polariser, $\sigma_\Lambda(\gamma_R)$, see vertical bars in Fig. 2, which we compare to the fitted σ_Λ for linear polarisation shown as crosses. We recall that the electric field at the sample has both in-plane and out-of-plane components, and we consider^{35,52} the relative strengths of the components along the x , y , and z axes, respectively as $E = [E_x, E_y, E_z]$. The intensity in the back focal plane (BFP) of the condenser varies spatially, with a maximum at the center, determined by the lamp, diffuser and lenses in the illumination path, as characterised in our previous work.³⁵ Using the known spatial dependence, we can calculate the intensity components at the sample polarised along the x , y , and z axes, normalized to have unity sum. For a linear polariser along x in the condenser BFP, we find $I_{\text{lin}} = [0.826, 0.007, 0.167]$, corresponding to field components $E_{\text{lin}} = [0.909, 0.084, 0.409]$ given by the square root of the intensity components. For radially polarised input to the BFP, we have $I_{\text{rad}} = [0.333, 0.333, 0.334]$ corresponding to $E_{\text{rad}} = [0.577, 0.577, 0.578]$, showing that the z component is increased in the radially polarised case.

For a spherical NP, the polarisation direction should not

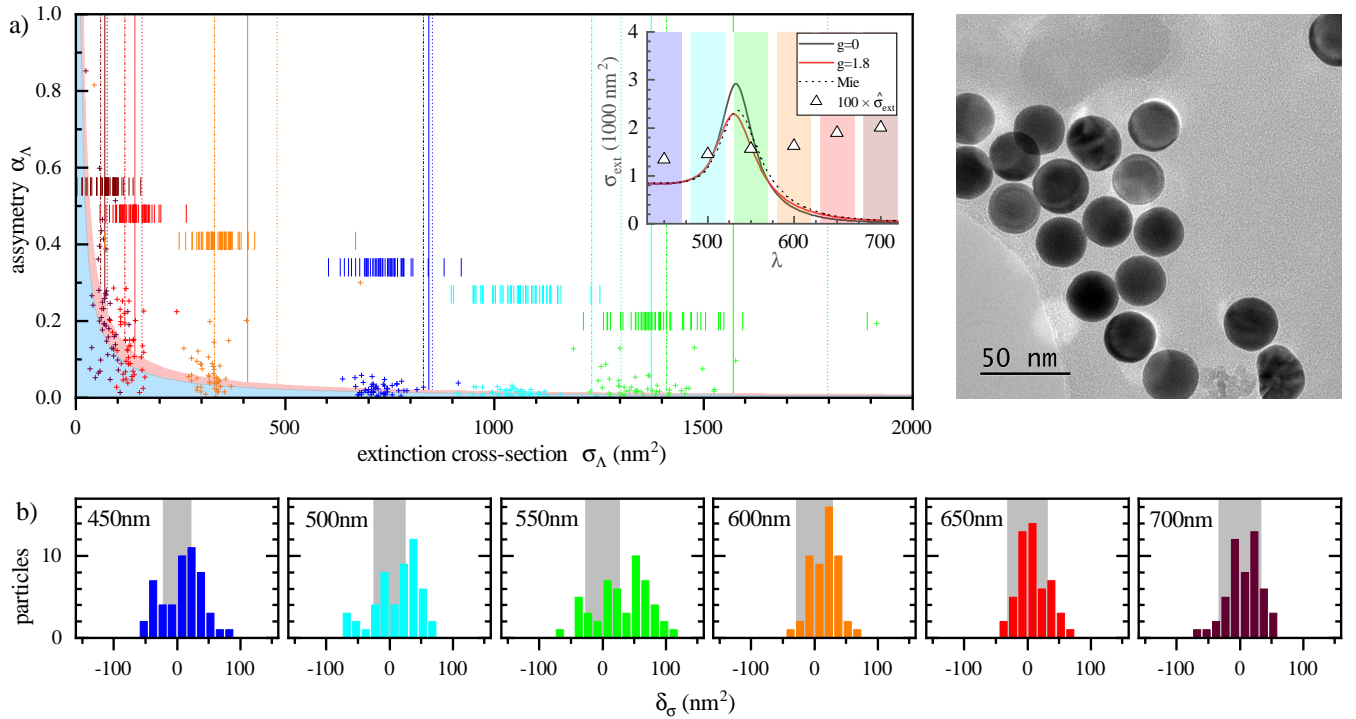


FIG. 2. Measured properties of $N = 51$ UGNs of $D = 30\text{nm}$ nominal diameter. a) Asymmetry α_Λ versus cross-section σ_Λ for $\Lambda = \{450\text{nm}, 500\text{nm}, 550\text{nm}, 600\text{nm}, 650\text{nm}, 700\text{nm}\}$, color-coded to reflect the center wavelength. Coloured crosses indicate the fitted parameters for linear polarisations using Eq. 9. Coloured vertical bars indicate the measured $\sigma_\Lambda(\gamma_R)$ for radial polarisation, at vertical positions chosen for clarity. A representative TEM image^{43,44} of NPs from the same batch is shown on the right. The noise in α_Λ is shown as shaded areas for $\Lambda = 450\text{nm}$ (bluish) and $\Lambda = 700\text{nm}$ (reddish), estimated as $(\hat{\sigma}_{\text{ext}}/\sqrt{1.5})/\sigma_\Lambda$, corresponding to the lowest and highest noise versus Λ , respectively. See Sec. C for further details about the noise in the fit parameters. Solid vertical lines indicate the calculated σ_Λ for a spherical gold NP for each Λ , taking into account averaging over filter ranges, for the sample-averaged TEM diameter D_V , 27.94nm , and the OL permittivity dataset with $g = 1.8$. The corresponding spectrum is given in the inset, showing additionally the case $g = 0$. Dotted vertical lines indicate the same as solid, but calculated using Mie theory. Dash-dotted lines indicate the same as dotted, but for MP permittivity. The corresponding spectrum is shown by the dotted curve in the inset. Vertical colour bands indicate the filter ranges used in the experiment. The measurement error $\hat{\sigma}_{\text{ext}}$, polarisation-averaged and FOV-averaged, are shown for each Λ , scaled by a factor 100. b) Histograms of δ_σ , for each Λ as labelled, with gray bands showing $\pm\sqrt{2}\hat{\sigma}_{\text{ext}}$, where the $\sqrt{2}$ factor accounts for the additional noise arising from the subtraction in δ_σ .

affect the measured σ_{ext} , and thus we expect the difference $\delta_\sigma = \sigma_\Lambda(\gamma_R) - \sigma_\Lambda$ to be negligible. The histograms of δ_σ are shown in Fig. 2b, and we find for channels with large cross-sections $\Lambda = \{450, 500, 550\}$ a shift towards $\delta_\sigma > 0$ of relative magnitude $\delta_\sigma/\sigma_\Lambda$ below 3%, while for the other channels δ_σ is dominated by noise, shown as gray bars. To explain this small shift, we recall the “long shadow” effect,⁵⁵ which arises from the illumination covering an oblique angular range while referencing to the intensity transmitted through the imaged sample plane. The NA of the condenser and the intensity distribution in its BFP provide the weighting of the illumination angles at the sample, from which we calculate the long-shadow factor used. However, the transmission of the condenser and objective for oblique angles is polarisation-dependent, due to the reflections on the lens surfaces, which are generally lower for p polarisation compared to s polarisation. Radial polarisation is purely p polarised, while linear polarisation contains equal parts of s and p polarised light. Considering that the long-shadow factor is increasing with incidence angle,⁵⁵ the higher transmission at higher angles for

radial polarisation creates an illumination with a higher long-shadow factor. This systematic error can be approximately compensated by reducing the measured $\sigma_\Lambda(\gamma_R)$ by a factor 0.97, having an effect explored below. One could also speculate that a preferential orientation of the NPs on the surface creates the difference. However, we would expect in such a case that NPs preferentially lie flat on the surface, providing a larger binding surface, which would lead to a higher cross-section for in-plane fields, opposite to what is observed.

B. Morphometric analysis

We introduced the morphometric analysis method, i.e. solving the inverse problem, in Ref. 43. We summarize the key points here. σ_{sca} and σ_{abs} are discretely calculated over a multidimensional space with parameters $(b/a, c/a, \phi, \theta, \psi)$, where the illumination intensity spectra of the color channels Λ and the selected permittivity are taken into account. We then generate interpolants for σ_{sca} and σ_{abs} using the calcu-

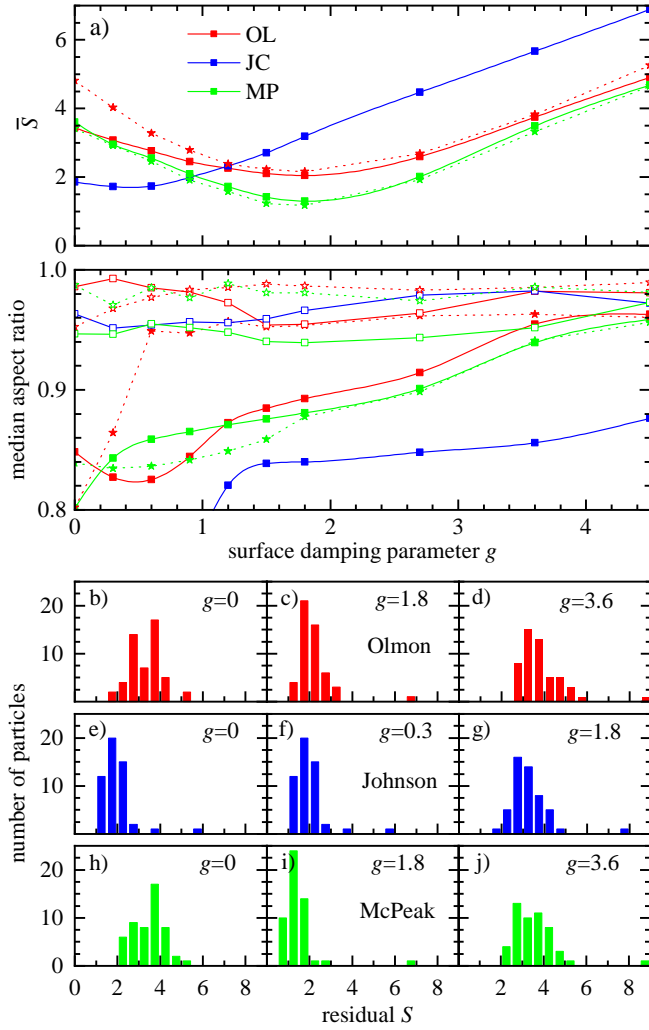


FIG. 3. \bar{S} and selected statistics of S for $N = 51$ UGNs of nominal $D = 30\text{nm}$ for varying surface damping parameter g and different ϵ datasets as indicated by color. (a) Top: \bar{S} versus g . Solid lines and squares for $\epsilon_{\text{NP}}(\lambda)$. Dotted lines and stars for $\epsilon_{\text{NP}}^s(\lambda)$ with $0.97 \times$ correction for $\sigma_{\text{ext}}(\gamma_{\text{R}})$ data. Bottom: median of the fitted average aspect ratio, for MAR (filled symbols) and PAR (empty symbols). Solid and dotted line designations same as Top. (b–j) Histograms of S , with (b–d) using the OL dataset with $g = \{0, 1.8, 3.6\}$, (e–g) JC dataset with $g = \{0, 0.3, 1.8\}$, (h–j) MP dataset with $g = \{0, 1.8, 3.6\}$. The values of g shown are at $g = 0$, the minimum of $\bar{S}(g)$ and a larger g .

lated grid. We compare the measured values of a given particle i to the calculated values for each point on the grid using the normalized error,

$$S^2 = \frac{1}{n} \sum_{\gamma, \Lambda} \left(\frac{\sigma_{\Lambda}(\gamma_{\text{P}}) - \sigma_{\text{abs}, \Lambda}(\gamma_{\text{P}}) - \eta \sigma_{\text{sca}, \Lambda}(\gamma_{\text{P}})}{\hat{\sigma}_{\Lambda}(\gamma_{\text{P}})} \right)^2, \quad (11)$$

where we dropped the index i for brevity. n is the number of measurements in the sum, which includes the radially polarised measurement $\gamma_{\text{P}} = \gamma_{\text{R}}$, and $\hat{\sigma}_{\Lambda}(\gamma_{\text{P}})$ is the measurement noise associated with $\sigma_{\Lambda}(\gamma_{\text{P}})$. The factor η is the fraction of scattered light which is not collected by the objective and thus

contributes to the measured extinction. For our experimental configuration we calculated⁵⁴ $\eta = 0.646$.

Since the right side of Eq. 11 is a fourth-order polynomial in V we can minimise S^2 with respect to V analytically to obtain S and V for the specific dataset and obtain the volume-equivalent diameter, $D_V = \sqrt[3]{6V/\pi}$. Points on the grid where S^2 is smaller than a suitable cut-off are then used as initial guesses for a gradient descent employing the σ_{sca} and σ_{abs} interpolants, each providing a solution. We use the solution with the minimum S^2 as descriptor of the morphometry and orientation of the NP. To constrain retrieved morphometries, we have previously applied additional penalties using prior knowledge, e.g. ensemble specifications from the NP manufacturer. We do not implement this here to avoid the influence of systematic errors in such specifications.

The six spectral channels used improves the interrogation of the LSPR spectral shape compared to Ref. 43. Hence, we re-examine here the best choice of the permittivity ϵ_{NP} , defined by the minimum of

$$\bar{S} = \sqrt{M\{S^2\}}. \quad (12)$$

Since S is normalized by $\hat{\sigma}_{\text{ext}}(\gamma_{\text{P}})$ in Eq. 11, we would expect $S = 1$ for the correct model, without taking into account the number of fit parameters and the number of data points to be fitted per NP. Considering that we use $p = 6$ free parameters to fit the $n = 30$ measurements (four linear and one radial polarisation at 6 wavelengths), this expectation is reduced by the number of degrees of freedom $n - p$ to $S \approx \sqrt{(n - p)/n} \approx 0.9$.

\bar{S} is shown for the data analysis as discussed to this point by the solid curves in Fig. 3a as a function of the surface damping parameter g for each of the experimental ϵ datasets. We find minimum values of $\bar{S} = 1.29$ at $g = 1.8$ for the MP dataset, $\bar{S} = 2.05$ at $g = 1.8$ for the OL dataset, and $\bar{S} = 1.72$ at $g = 0.3$ for the JC dataset. Compared to our results in Ref. 44, \bar{S} is more sensitive to g , due to the lower noise and larger number of measurements used. The histograms of S are shown in Fig. 3 for each dataset and g at the minimum of $\bar{S}(g)$ and either side of it. At the minimum, a nearly Gaussian shape is observed. The distributions of S for each dataset display a few outliers of large S , indicating some NPs are not well described by the model.

Notably, the smallest \bar{S} is found for MP, which indicates the best choice since it represents the model which best fits the data. On the other hand, we see in Fig. 3, 12, and 13, that OL retrieves the roundest shapes as shown by $M\{\text{MAR}\}$, closest to the shape measured in TEM. Excluding the radial polarisation data yields the lowest \bar{S} , for all permittivities (see Fig. 12). This can be rationalised noting that the radial polarisation probes the shape in the out-of-plane direction, restraining the fit from using this shape to create spectral shifts while the in-plane shape is constrained by $\sigma_{\Lambda}(\gamma_{\text{P}})$.

In principle, all permittivity datasets should be consistent apart from surface damping, as they have all been measured on gold films of different crystallinity. While this is the case for OL and JC, with JC corresponding to OL with $g \approx 1$, reflecting the lower crystallinity of the film measured in JC compared to the single crystal data in OL, MP corresponds to a

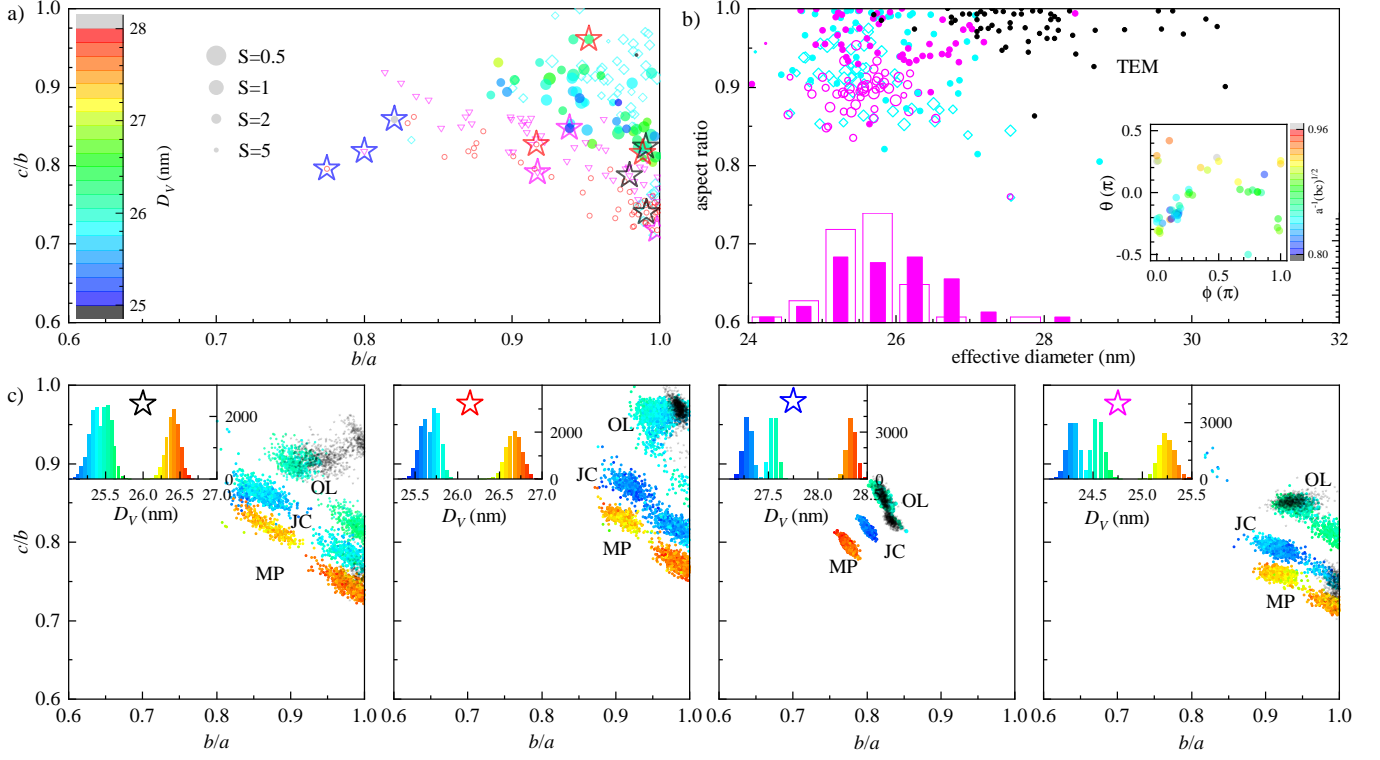


FIG. 4. Morphometric results for $N = 51$ nominally $D = 30$ nm UGNs. (a) Retrieved ARs for OL $g = 1.8$ are shown as filled symbols with a colour indicating the fitted diameter D_V . ARs retrieved using only $\sigma_\Lambda(\gamma_P)$ are shown as cyan empty diamonds. Also shown are retrieved ARs for JC $g = 0.3$, (magenta empty triangles), and for MP $g = 1.8$ (red empty circles). (b) MAR versus D_V for OL $g = 1.8$ (magenta empty circles), with the histogram showing the number distribution of D_V (empty) and D_P (filled). Corresponding PAR are shown as filled symbols versus D_P . Results using only $\sigma_\Lambda(\gamma_P)$ are shown as diamonds. The black filled squares indicate TEM measurements PAR versus D_P . Inset: pitch (θ) and roll (ϕ) angles showing the particle orientation for OL, with a symbol colour encoding the MAR. The size of the circles in (a) and the empty symbols in (b) is given by $S^- = 1/(1+S)$, as indicated in (a), with larger size indicating lower fit error S . (c) Simulated effect of the measurement noise on the retrieved ARs for individual NPs indicated by the colored stars in (a). Results for 1000 realisations of Gaussian noise with σ_{ext} standard deviation added to the measured extinction data are shown. Inset: D_V histograms, providing a colour scale for the symbols. Results for OL, JC, and MP at g of 1.8, 0.3, and 1.8, respectively, with corresponding results labelled. Black symbols are results using only $\sigma_\Lambda(\gamma_P)$ for OL.

higher plasma frequency, leading to a blueshift of the LSPR of a spherical NP by about⁴⁴ 4 nm. Using MP in the fit thus yields higher NP asymmetry, which compensates the blueshift by a redshift due to non-spherical shape.

The results of the morphometric fits for the $N = 51$ nominally $D = 30$ nm UGNs are shown in panels (a–b) of Fig. 4. The retrieved NP shapes for OL $g = 1.8$, shown as filled circles, are slightly non-spherical, with $c/b = 0.91 \pm 0.032$, $c/a = 0.82 \pm 0.12$, and $b/a = 0.96 \pm 0.04$, where the errors are standard deviations of the ensemble, and a mean (median) MAR of 0.89 (0.90). When excluding $\sigma_\Lambda(\gamma_R)$, the results show slightly rounder NP shapes, with $c/b = 0.88 \pm 0.07$, $c/a = 0.85 \pm 0.07$, $b/a = 0.97 \pm 0.03$, and a mean (median) MAR of 0.91 (0.91). Here, the shapes form two clusters, with the smaller cluster having c/b lower than any shapes retrieved when including $\sigma_\Lambda(\gamma_R)$. We find $D_V = (25.6 \pm 0.5)$ nm (median 25.6 nm) over the ensemble when including $\sigma_\Lambda(\gamma_R)$, showing a systematic deviation of about 2 nm, or 8%, to the TEM results. The results for the JC and MP datasets generally show retrieved shapes which are more widely distributed and

of stronger non-sphericity compared to OL, and MP retrieves nearly 1 nm larger average diameters. We explore in Sec. E the effect of the different corrections and selections introduced on the shape retrieval in more detail.

Notably, the projected shapes are generally rounder and of larger diameter, see filled circles (PAR) and filled histogram (D_P) in Fig. 4b. This can be interpreted in two ways: (i) since the in-plane asymmetry is measured with higher precision via the γ_P dependence, the PAR has less error and thus reflects the correct aspect ratio in all three dimensions of the NP, (ii) the NPs are orientated on the surface in a way to appear more round in-plane. Considering the nearly spherical shapes, a physical mechanism which would result in (ii) both for TEM and optical measurements is not obvious.

In Fig. 4c, we examine the uncertainty in the retrieved ARs and D_V due to measurement noise for four selected NPs, indicated by the colored stars in Fig. 4a. The analysis was done for all three permittivity datasets with g minimizing \bar{S} . We simulate the effect of the measurement noise by adding a realisation of Gaussian random noise with a standard deviation

of $\hat{\sigma}_\Lambda(\gamma_p)$ (see inset of Fig. 2a) to the measured $\sigma_\Lambda(\gamma_p)$, and then repeat the morphometric analysis. Each set of scatter data in each of the four panels represents 1000 noise realizations. The ARs often exhibit bimodal distributions, with the greatest separation between modes apparent for MP and JC, while the width of the individual modes is typically below 5%. Notably, the modes often are close to $b = a$ or $c = b$, allowing to achieve zero in-plane asymmetry (which is defined with high precision by the linear polarisation data) for appropriate NP orientations. Using synthetic σ_{ext} data generated using the Rayleigh-Gans model and the specified experimental corrections, such multimodal results are not observed,⁴³ suggesting that they are caused by systematic measurement errors. Notably, the sample distributions in Fig. 4a for each permittivity mirrors the spread of the noise distributions for the rounder NPs in Fig. 4c for each permittivity, which points to a homogeneity of the sample, as well as this systematic effect. We will return to this topic again later in the text. Generally, for near-spherical NPs, AR retrieval is less precise due to the quadratic parameter dependencies close to symmetry points of the multi-dimensional parameter space.⁴³ Significantly asymmetric NPs instead yield more precise retrieval, as exemplified by the blue-starred NP. In this case, precision is better than 3%, corresponding to 0.84 nm length along the NP axes. For further insights into this effect, see Sec. C. Variations in n_m result in systematic changes in c/b of about twice the index change, as discussed in Sec. F. For a realistic refractive index accuracy of 0.01, the corresponding c/b systematic error is 2%. Remarkably, the retrieved D_V shows a precision of (0.04 – 0.1) nm standard deviation for the selected NPs.

The systematic deviation of about 2nm between the mean of the retrieved D_V and that found by TEM might be due to several factors. A known systematic error is the quasi-static approximation used in the model. Considering the wavelength in vacuum of the LSPR for a spherical gold NP of about $\lambda_0 = 530\text{nm}$, the wavelength in the medium of $n_m = 1.52$ is $\lambda_0/n_m \approx 350\text{nm}$, which is about 12 times the nominal diameter of the NPs. This suggests that taking into account retardation, which leads to radiative damping and red-shift of the LSPR, might be relevant to achieve accuracies below 10% for the investigated NPs. Indeed, the extinction spectrum of a gold NP with the TEM-measured average diameter $D_V = 27.94\text{nm}$, calculated including retardation using Mie theory (see inset of Fig. 2a, dotted black line), shows an about 4% increase and 5 nm red-shift of the LSPR peak, see also Sec. G. The vertical lines in Fig. 2a show the corresponding weighted cross-sections (solid for Rayleigh-Gans, dotted for Mie) for all colour channels. We would expect that the red-shift would result in rounder retrieved NPs, while the increase would result in an about 1% smaller D_V considering the approximate scaling of the cross-section with the volume.

To investigate this further while keeping the Rayleigh-Gans model, we approximate the effects of retardation by spectrally shifting the permittivity with respect to λ to obtain $\epsilon_{\text{NP}}^s(\lambda) = \epsilon_{\text{NP}}(\lambda + \delta\lambda)$, with $\delta\lambda = -5\text{nm}$, and repeating the ON analysis using ϵ_{NP}^s and the $0.97\times$ correction for $\sigma_{\text{ext}}(\gamma_R)$. The resulting dependence of \bar{S} and the median MAR on g is given as dotted lines in Fig. 3a for OL and MP, show-

ing that the g at which \bar{S} reaches a minimum is rather unaffected, while the median MAR increases. The corresponding ON results are given in Fig. 5 for OL and MP. The retrieved shapes are rounder for both datasets, with OL showing clearly round shape retrieval with median MAR of 0.954, compared to 0.892 for MP. Meanwhile, the median diameter for MP is $M\{D_V\} = 26.72\text{nm}$, larger than 25.77 nm for OL. For OL, nearly all of the asymmetry is in b/a corresponding to a prolate particle, and most orientations show $\theta \approx -\pi/2$, corresponding to a prolate NP standing on end, i.e. its long axis is normal to the surface. This suggests a systematic effect, where a negligible in-plane polarisation-dependence combines with a constrain by $\sigma_{\text{ext}}(\gamma_R)$. MP by comparison shows a less constrained distribution of orientations, with widely distributed tilts θ .

The projected aspect ratios PAR versus the corresponding diameters D_p are also shown in Fig. 5b. The median PAR is $M\{\text{PAR}\} = 0.987$ for OL and 0.981 for MP, with its dependence on g given in Fig. 3a. These values are significantly higher than those of MAR. The histograms of D_p are shown and the median for MP is $M\{D_p\} = 27.02\text{nm}$, larger than 25.37, nm for OL. Remarkably, both PAR and D_p for MP are in good agreement with the TEM results ($M\{\text{PAR}\} = 0.985$, $M\{D_p\} = 27.75\text{nm}$).

Furthermore, for the two rounder particles in Fig. 5c, OL shows distinctly bimodal distributions, while MP returns unimodal distributions. For these examples, at one standard deviation from the mean, the precision in D_V is improved to (0.04 – 0.07) nm, and the precision in AR is (0.37% - 2.8%) for OL and (0.45%-2%) for MP, depending on the NP.

V. CONCLUSIONS

We have presented an enhanced ON method with optical cross-sections measured using six spectral channels, and both linear and radial polarisation to probe both in-plane and out-of-plane NP response. For nominally 30nm ultra-uniform gold nanospheres, we demonstrated significant improvement in the precision and accuracy of the method. Precision in the size and shape has been improved to below 0.1 nm and 5%, respectively. We examined the effect of the permittivity dataset on the morphometry retrieval and found that McPeak *et al.*⁴⁶ with surface damping factor $g = 1.8$ yields the best results. We find that the small effect of retardation for these NP, which are some 12 times smaller than the light wavelength in the surrounding medium, provides a LSPR red-shift of some 5nm. This is significant due to the high precision of the measurements, and correcting for it improves accuracy to within 5% in shape and size using TEM measurements as reference. We however note that this accuracy is contingent on the permittivity used to describe the material response.

Future development could see the use of numerical models, capable of treating particles outside of the limitations of analytical models. Another approximation limiting the accuracy is the use of a local permittivity to describe the nanoparticle optical response, which is known to break down on the sub-nm scale in general. Again, more complex theory models⁵⁶

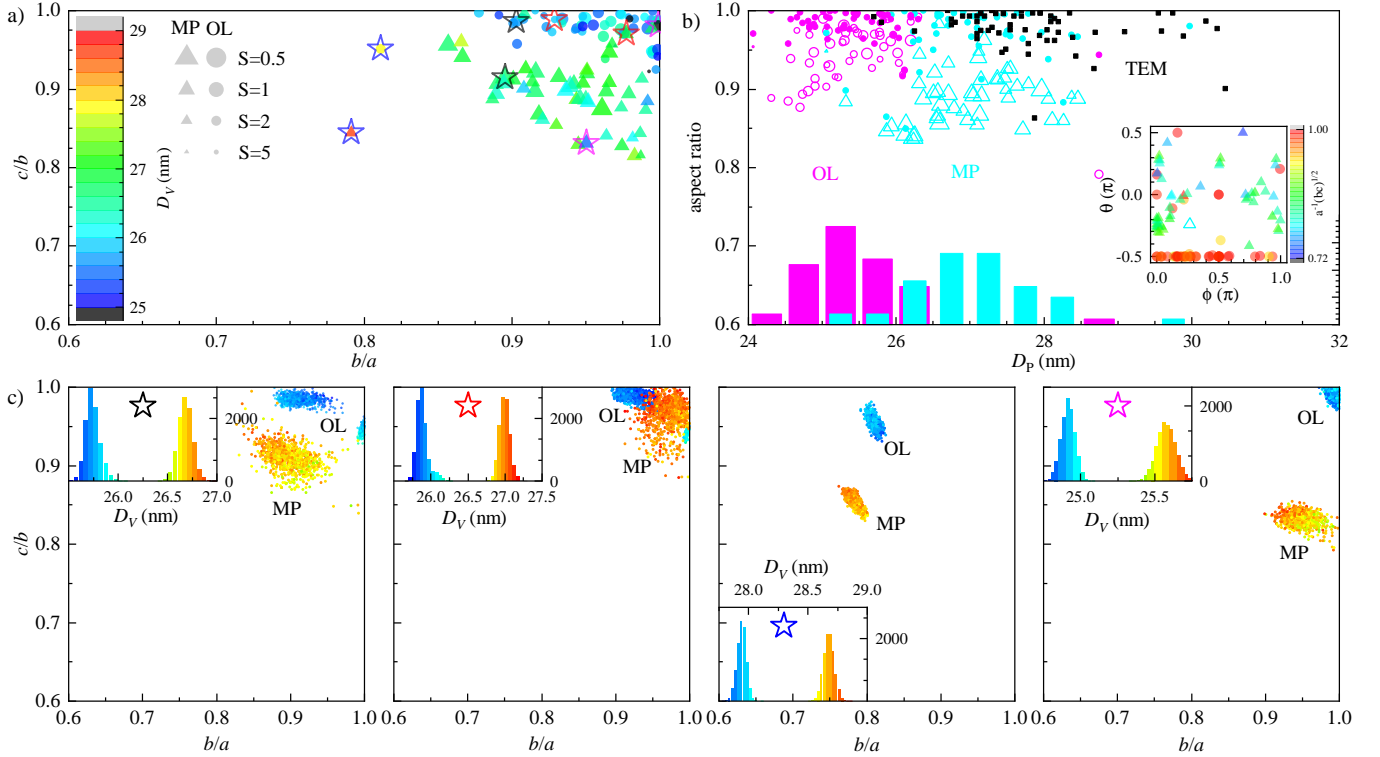


FIG. 5. Similar to Fig. 4, but for OL and MP using $\epsilon_{\text{NP}}^s(\lambda) = \epsilon_{\text{NP}}(\lambda + \delta\lambda)$ with $\delta\lambda = 5$ nm and the $0.97\times$ correction for $\sigma_{\text{ext}}(\gamma_{\text{R}})$. (a) Retrieved ARs shown as filled symbols (MP triangles, OL circles) with a color indicating the fitted diameter D_V . (b) MAR (empty symbols) and PAR (filled symbols) versus D_p , with the histogram showing the number distribution of D_p , with OL shown as magenta circles/bars and MP as cyan triangles/bars. The black filled squares indicate TEM measurements PAR versus D_p . Inset: pitch (θ) and roll (ϕ) angles showing the particle orientation. (c) Simulated effect of the measurement noise on the retrieved ARs for individual NPs indicated by the colored stars in (a). Results for 1000 realisations of Gaussian noise with $\hat{\sigma}_{\text{ext}}$ standard deviation added to the measured extinction data are shown. Inset: D_V histograms, providing a colour scale for the symbols.

can be used to improve on this. The precision of the method is so high that small systematic effects in the experimental setup, such as the angular resolved transmission and the angular intensity distributions, are relevant to achieve an accuracy comparable to, or better than, the precision. These can be corrected by further characterisation of the instrumentation.

Overall, this study shows the ability of the ON to complement TEM, and as a stand-alone methodology for accurate NP morphometric studies. It also offers an interesting approach to determine the permittivity of materials on the nanoscale, and to uncover non-local effects.

ACKNOWLEDGMENTS

F.A. thanks Al-Furat Al-Awsat Technical University (ATU) for the financial support toward her Ph.D. studies. Parts of this work were funded by the UK Research Council EPSRC Impact Acceleration Account of Cardiff University. The microscope set-up was supported by the UK Research Council EPSRC (grants n. No. EP/I005072/1 and EP/M028313/1). We thank Iestyn Pope for technical support in the experiments and in hardware development of the radial polariser.

AUTHOR CONTRIBUTIONS

L.P., W.L. and P.B. conceived the work. F.K. prepared the samples and performed the optical measurements. L.P., P.B. and W.L. developed the numerical model and fitting methods. L.P. performed the numerical simulations and data fitting. All authors contributed to the data interpretation and writing of the manuscript.

Appendix A: Illumination spectrum and camera sensitivity

The illumination setup in this experiment uses a halogen lamp as source, operated at close to max setting (100 W), with 40 nm bandwidth filters to provide coarse wavelength selection in the experiment. While the filters exhibit close to flat transmission across their bandwidth, the lamp spectrum is varying over the filter ranges, specifically in the green-blue region. To take this into account, we approximate the lamp spectrum as a blackbody radiator as in Section 2.1.4 of Ref. 54. One must also consider the spectral properties of the detection. The PCO Edge 5.5 scientific CMOS (sCMOS) exhibits a quantum efficiency (QE) depending on wavelength, which

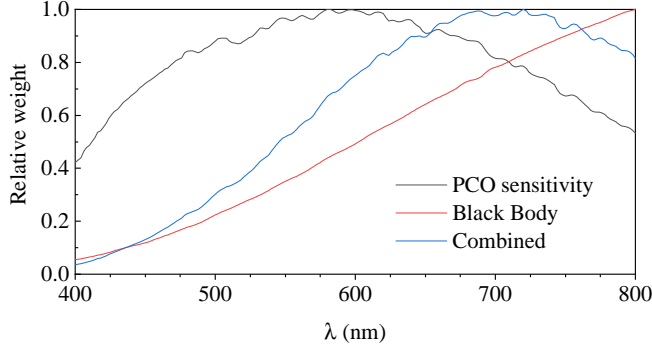


FIG. 6. Plot of $l(\lambda)$ (red curve), $c(\lambda)$ (black curve), and $w(\lambda)$ (blue curve).

was characterised by the manufacturer and was digitised for this work. Fig. 6 shows the calculated blackbody lamp spectrum $l(\lambda)$, the camera sensitivity $c(\lambda)$, and the combined dependence $w(\lambda) = l(\lambda)c(\lambda)$, normalized for visualisation purposes.

Appendix B: Projected ellipsoidal parameters

Given the rotation angles (ϕ, θ, ψ) and semi-axis lengths (a, b, c) of the fitted ellipsoid, as introduced in Sec. II, we can calculate its projection along the z axis in the laboratory frame, which is normal to the substrate surface, as follows.⁵⁷ We introduce the ellipsoid matrix

$$M = \begin{bmatrix} a^{-2} & 0 & 0 \\ 0 & b^{-2} & 0 \\ 0 & 0 & c^{-2} \end{bmatrix} \quad (\text{B1})$$

describing the ellipsoid surface as points \mathbf{r} respecting $\mathbf{r} \cdot M \mathbf{r} = 1$, and rotate it into the lab frame,

$$RMR^T = \begin{bmatrix} A & \mathbf{b} \\ \mathbf{b}^T & d \end{bmatrix} \quad (\text{B2})$$

using the rotation $R = R_\psi R_\theta R_\phi$ as introduced in Sec. II. The rotated matrix is expressed by an in-plane matrix A , a vector \mathbf{b} , and a scalar d as shown. We proceed by introducing the projected ellipse matrix

$$Q = A - \frac{\mathbf{b}\mathbf{b}^T}{d} \quad (\text{B3})$$

which we diagonalise to determine its two eigenvalues $\lambda_1 < \lambda_2$, which define the in-plane semi-axis lengths $a' = 1/\sqrt{\lambda_1}$ and $b' = 1/\sqrt{\lambda_2}$.

Appendix C: Noise of linear polarisation fit parameters

The extinction cross-sections, σ_{ext} , measured for different linear polariser angles, γ_p , are fitted with Eq. 9 to retrieve the

in-plane dipolar asymmetry, α , its orientation, γ , and the average cross-section, σ .

To determine how the experimental noise, $\hat{\sigma}_{\text{ext}}$ arising from photon noise and sample background structure, affects the fit parameters, we simulate realisations of $\sigma_{\text{ext}}(\gamma_p)$ for $N_p \in [3, 4, 6]$, asymmetries $\alpha_s \in [0, 0.1, 0.2, 0.3, 0.4, 0.5, 0.8, 1.0]$, and orientations $\gamma_s \in [0, 10, 15, 20, 30, 45, 90]$ degrees. We generate $\sigma_{\text{ext}}(\gamma_p, \alpha_s, \gamma_s)$ by adding Gaussian noise of standard deviation $\hat{\sigma}_{\text{ext}} = 0.1\sigma$ to the results of Eq. 9, and fit the data using Eq. 9, for $N = 10000$ noise realisations.

For small asymmetries α_s , σ is effectively the mean of $\sigma_{\text{ext}}(\gamma_p)$ over all γ_p , so that the noise in σ should be given by $\hat{\sigma}_{\text{ext}}/\sqrt{N_p}$, where N_p is the number linear polariser angles used. We accordingly define an effective number of measurements $n(\alpha_s, \gamma_s) = (\hat{\sigma}_{\text{ext}}/\hat{\sigma})^2$ for σ , and the simulation results shown in Fig. 7 confirm that n is close to N_p , notably not only for $\alpha_s = 0$, but across all α_s .

For α , the effective number of measurements is defined as $n(\alpha_s, \gamma_s) = (\hat{\sigma}_{\text{ext}}/(\sigma\hat{\alpha}))^2$, noting that the oscillation amplitude is $\sigma\alpha$, and the simulation results are shown in Fig. 8. Naively, one could expect $n = N_p - 2$, considering that we measure 2 additional parameters apart from α . This is also approximately the case for α_s around 0.3-0.5. For small $\alpha_s < 0.3$, n increases, reaching about twice that value at $\alpha_s = 0$. This is attributed to the choice $\alpha \leq 0$, controlling the sign of α by a 90 degree shift of the angle γ . Therefore, the distribution is narrowed, at the expense of noise in γ . For large $\alpha > 0.5$ instead, n decreases by about 1. We attribute this to a reduction of the noise in γ at the expense of the noise in α .

For γ , the noise $\hat{\gamma}$ is calculated in radians using a circular statistics⁵⁸ with the periodicity of 180 degrees, and the effective number of measurements is defined as $n(\alpha_s, \gamma_s) = 0.5(\hat{\sigma}_{\text{ext}}/(\sigma\alpha\hat{\gamma}))^2$, noting that the oscillation amplitude is given by $\sigma\alpha$. The simulation results shown in Fig. 9 indicate that n is about N_p , except for small α , where noise in γ becomes so large that $\hat{\gamma}$ is limited by the periodicity.

Interestingly there is no clear dependence of n on γ_s for any of the parameters, not even when measuring only $N_p = 3$ angles spaced by 60 degrees, indicating that using only 3 angles does not carry a precision penalty.

Appendix D: Influence of integration radius

The integration radius, r_i , affects the measurement of σ_{ext} in wide-field extinction microscopy. For simplicity, let us first consider the more straightforward case of darkfield microscopy, where scattering by a NP results in an intensity point spread function (PSF) in the image following ideally the two-dimensional (2D) Airy distribution; in reality there will be aberrations arising from the specific optics and polarisation dependent effects. The envelope of this distribution decays asymptotically to zero with the distance from the central peak, meaning that at any finite radius some of the scattered power is not captured. One must then correct the measured integral by a factor, for example based on the known fraction of the total integral. By contrast, in extinction we measure a coherent signal, given by the interference of the scattered light with

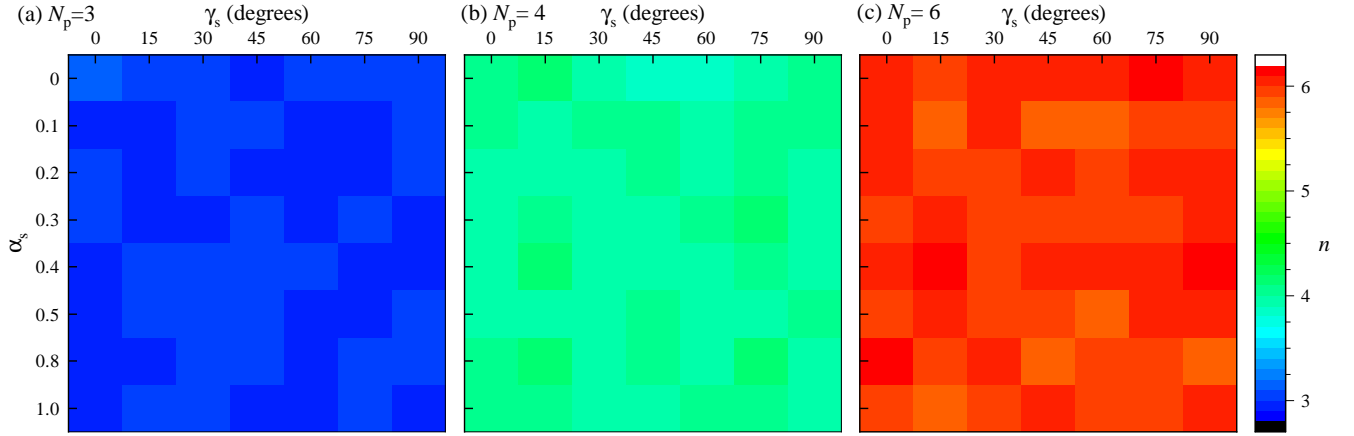


FIG. 7. Effective number of measurements n in the noise in σ , as function of α_s and γ_s , determined from fits to simulated extinction data using Eq. 9 ($n = (\hat{\sigma}_{\text{ext}}/\hat{\sigma})^2$, see text). Results are shown for 10% relative noise in σ_{ext} , for different numbers N_p of equidistant polariser angles across 180° , with panels (a), (b), and (c) using $N_p = 3, 4$, and 6 angles, respectively.

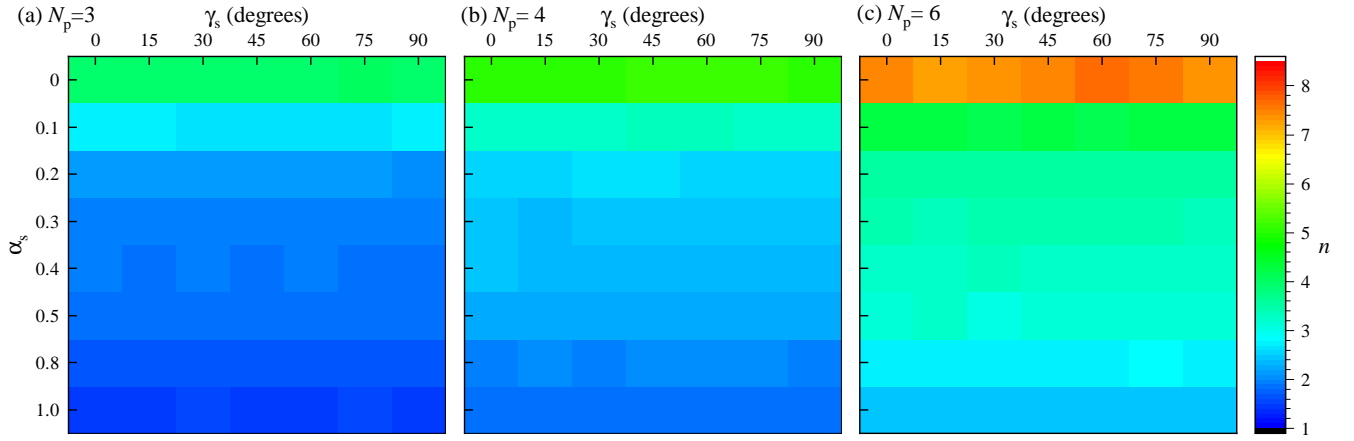


FIG. 8. As Fig. 7, but for α , using $n = (\hat{\sigma}_{\text{ext}}/(\sigma\hat{\alpha}))^2$.

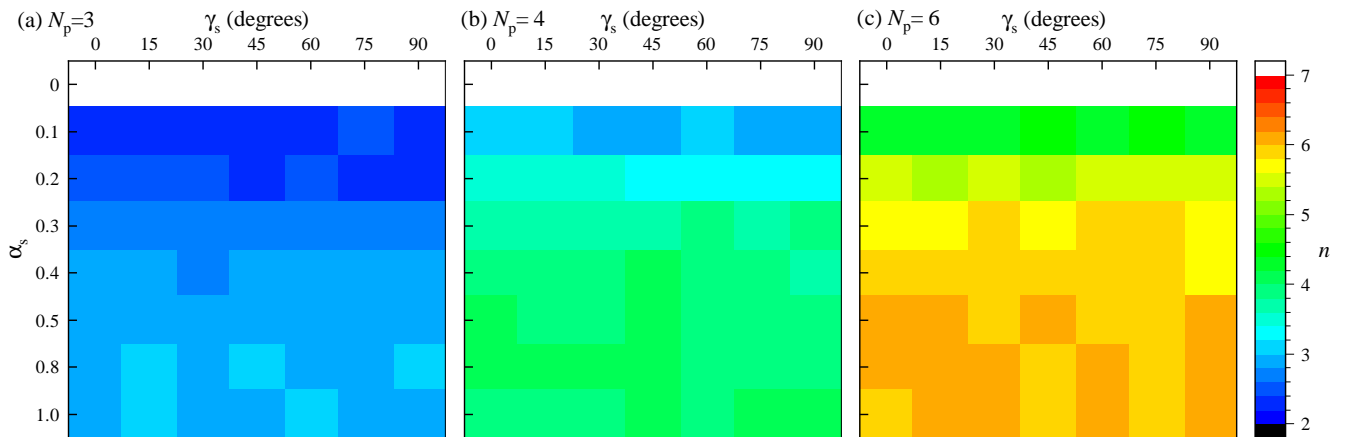


FIG. 9. As Fig. 8, but for γ , using $n = 0.5(\hat{\sigma}_{\text{ext}}/(\sigma\alpha\hat{\gamma}))^2$, with γ in radians, and $\hat{\gamma}$ calculated as circular error.⁵⁸

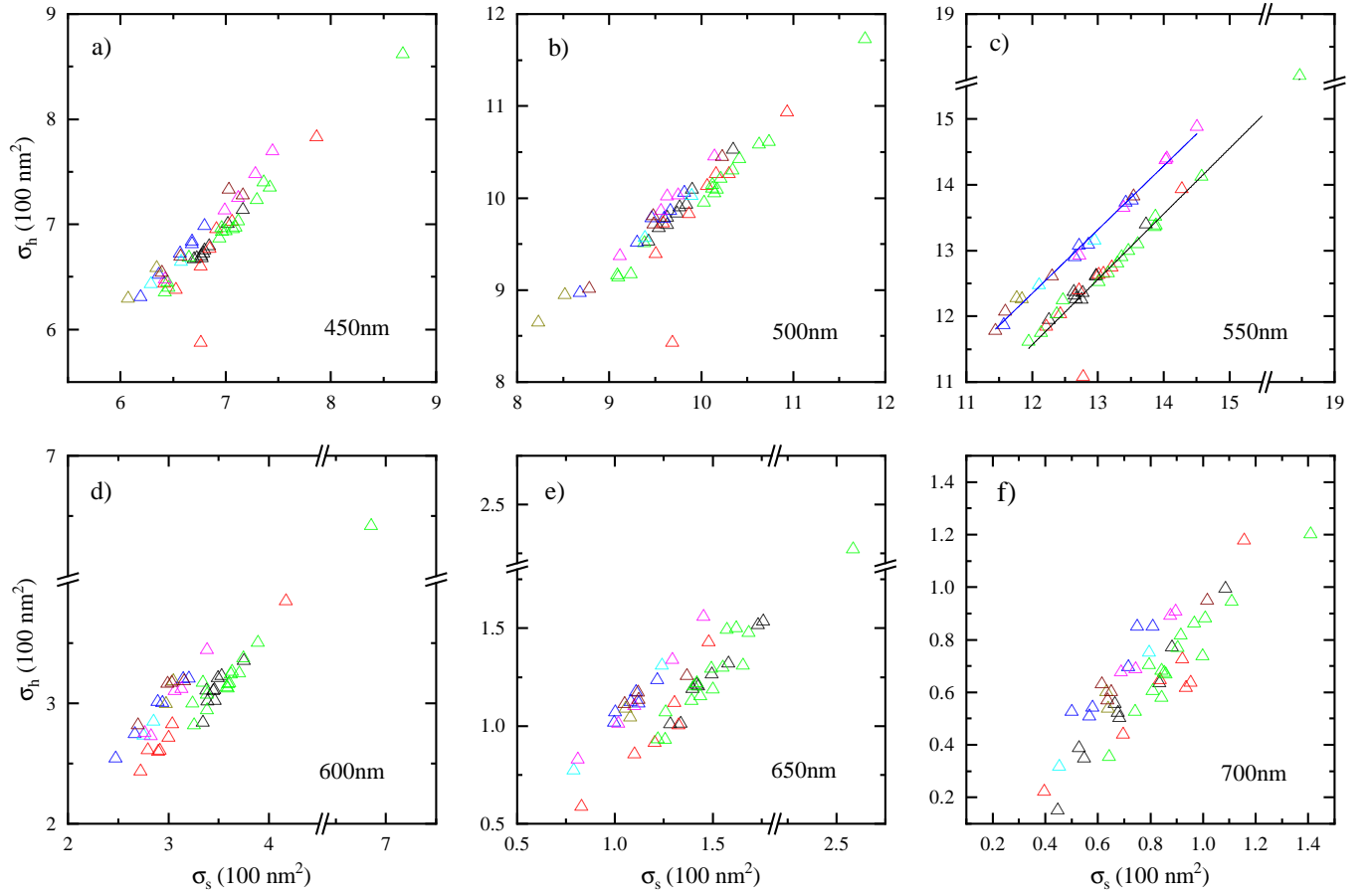


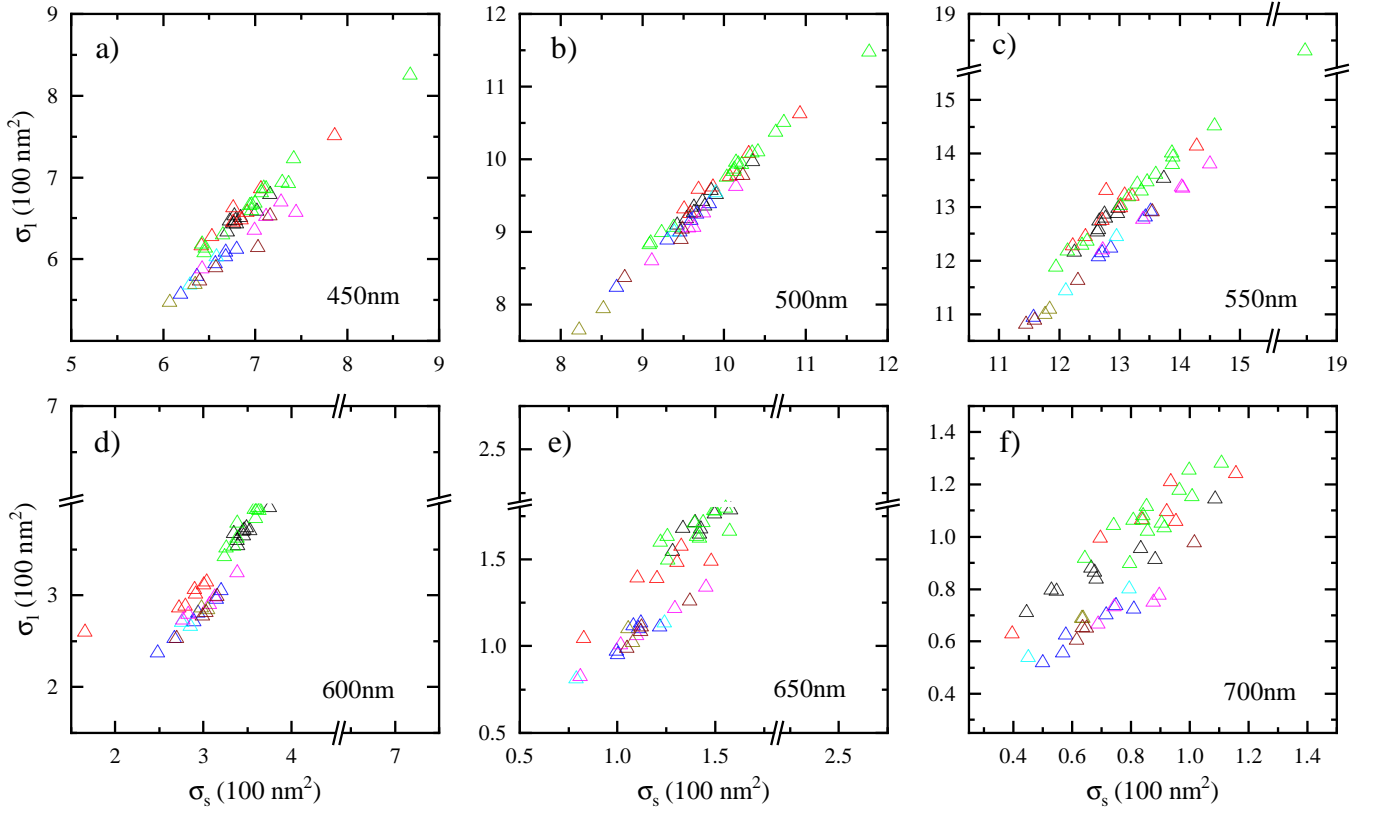
FIG. 10. Extinction cross-sections, σ_h , measured using the larger analysis radius, r_h as a function of the cross-sections, σ_s , measured using the standard analysis radius, r_s . Panels correspond to different filter center wavelengths in the experiment as (a) $\Lambda = 450\text{ nm}$, (b) $\Lambda = 500\text{ nm}$, (c) $\Lambda = 550\text{ nm}$, (d) $\Lambda = 600\text{ nm}$, (e) $\Lambda = 650\text{ nm}$, (f) $\Lambda = 700\text{ nm}$. Symbol colors (black, red, green, blue, cyan, magenta, dark yellow, dark red) indicate data associated to the 8 fields of view examined in the experiment. The linear fits observed in panel (c) serve to guide the eye along two clearly separated groups of datapoints.

the incident light in forward direction, an effect also called the optical theorem. This interference results in a more extended PSF determined by additional factors, specifically the in-plane coherence length of the illumination given by the numerical aperture of the condenser, and the defocus. We have shown previously⁵⁵ that for suitable choice of illumination NA one can achieve both a minimised fringing and therefore minimally extended PSFs, increasing the maximum possible area density of NPs in a sample, and a finite integration radius at which the extinction is fully measured.

In this work, we chose to use the maximum opening of the condenser ($\text{NA} = 1.34$) to maximised the out-of-plane component of the field at the sample, which we employ using radially polarised light to probe the out-of-plane shape of the NPs. However, using the maximum condenser NA leads to more extended fringing⁵⁵ in the extinction PSF, which decreases the maximum area density of NPs without spatially overlapping signals, and results in a measured extinction converging more slowly with integration radius. The latter point is the more important one for this work, since the sample area density of NPs was low. We typically use an integration ra-

dius, $r_s = 3\lambda/2\text{NA}$, which collects about 94% of the extinguished power (dependent on condenser/objective) for non-optimal NA selection. For the optimal conditions mentioned above, r_s would collect the full extinction, as the fringing at larger radii has compensating positive and negative contributions. Now, the discussed conditions are true assuming the particles are optimally focused, which for a purely absorbing NP can be considered to be the scenario when the peak extinction of the PSF is largest. When the focus is not optimal, the PSF spreads out, as the scattering changes its phase from being in-quadrature to the incident light, and thus not creating intensity changes, to being partly in or out of phase, creating bright and dark fringes (an effect which can be used to get contrast from non-absorbing scatters, popular in electron microscopy). In our data, a few fields of view (FOV) at a few Λ exhibit larger PSFs (10%-20% larger radius to first PSF minimum) compared to others, which should not be the case if all FOV are optimally focused. This implies that one should use $r_i > r_s$ to counter the defocus effects in the analysis of σ_{ext} .

In Fig. 10, we compare the polarisation-averaged σ_Λ measured using r_s , denoted as σ_s , and $r_h = 1.2r_s$, denoted as

FIG. 11. As for Fig. 10, but using the smaller analysis radius, r_l .TABLE I. $(\text{IQR}\{\sigma_l\} - \text{IQR}\{\sigma_s\})/\text{nm}^2$ as a function of Λ , with subscript $i \in (l, h)$, indicating which measurement radius, r_l or r_h , was used, and the IQR calculated over all $N = 51$ NPs from all 8 FOVs.

i	450 nm	500 nm	550 nm	600 nm	650 nm	700 nm
h	-5.47	-6.99	3.69	-23.02	-10.14	-2.21
s	7.49	11.28	6.10	33.00	21.67	10.74

σ_h . We do the same in Fig. 11, but for $r_l = 0.8r_s$. For both figures, symbol color indicates measurements from a single FOV. In Table I we see the difference between the interquartile ranges (IQR) of σ_s and σ_h or σ_l . Negative values across most FOV show that using r_h yields a smaller spread of the data, compared to r_s . The opposite is observed when using r_l where all values of the difference in IQR are positive, indicating an increase in the spread of data compared to r_s . For channels $\Lambda \in \{450, 500\}$ nm we can see that most of the data in Fig. 10 appears as a single group, specifically in σ_h , while for $\Lambda > 500$ nm two groups of data are visible, with black, red, and green triangles form the lower group, separating further from the rest for $\Lambda = 550$ nm and $\Lambda = 650$ nm. For $\Lambda = 700$ nm noise dominates. Note, the lines of best fit, added for $\Lambda = 550$ nm, indicate that certain FOVs are grouped together. We attribute this apparently wavelength- and FOV-dependent discrepancy to a slight defocus of the corresponding data. As might be expected from this attribution, the effect is more pronounced for σ_l in Fig. 11, since less of the signal is

integrated, such that a defocus in certain FOV would result in a greater deviation compared to the well-focused cases. One can easily observe that while the same wavelength-dependent separation of FOV is apparent, certain FOV (black, grey, red triangles) form an upper group already by $\Lambda = 450$ nm. A keen-eyed reader may note that this is the inverse behavior of σ_h , where these same FOV formed the upper group. However, this is an effect of the plotting; σ_s is plotted along the x -axis in both figures, however in Fig. 10, σ_s yields the smaller values of the two, while in Fig. 11, σ_s yields the larger values of the two.

Note, the data were taken with a sample reference shift of $s = 1550$ nm. For our experimental setup and $\Lambda = [450 \text{ nm}, 500 \text{ nm}, 550 \text{ nm}, 600 \text{ nm}, 650 \text{ nm}, 700 \text{ nm}]$, we have $2r_s = [931, 1035, 1138, 1241, 1345, 1448]$ nm, and $2r_h = [1117, 1241, 1366, 1490, 1614, 1738]$ nm. Already for $\Lambda = [650 \text{ nm}, 700 \text{ nm}]$, $2r_h > s$, which is not ideal due to partial integration of signal from the dark peak into that of the bright and vice versa, reducing the measured σ_{ext} . We see that using r_h does lead to a lower IQR at all Λ , except for $\Lambda = 550$ nm, where the defocus apparently was too large to be fully compensated. However the remaining discrepancy between the medians of the upper (five FOV) and lower (three FOV) groups of results for $\Lambda = 550$ nm is still only about 4% using r_h .

Overall, assuming a fixed s and sample density, this examination indicates that in future, one could optimize the illumi-

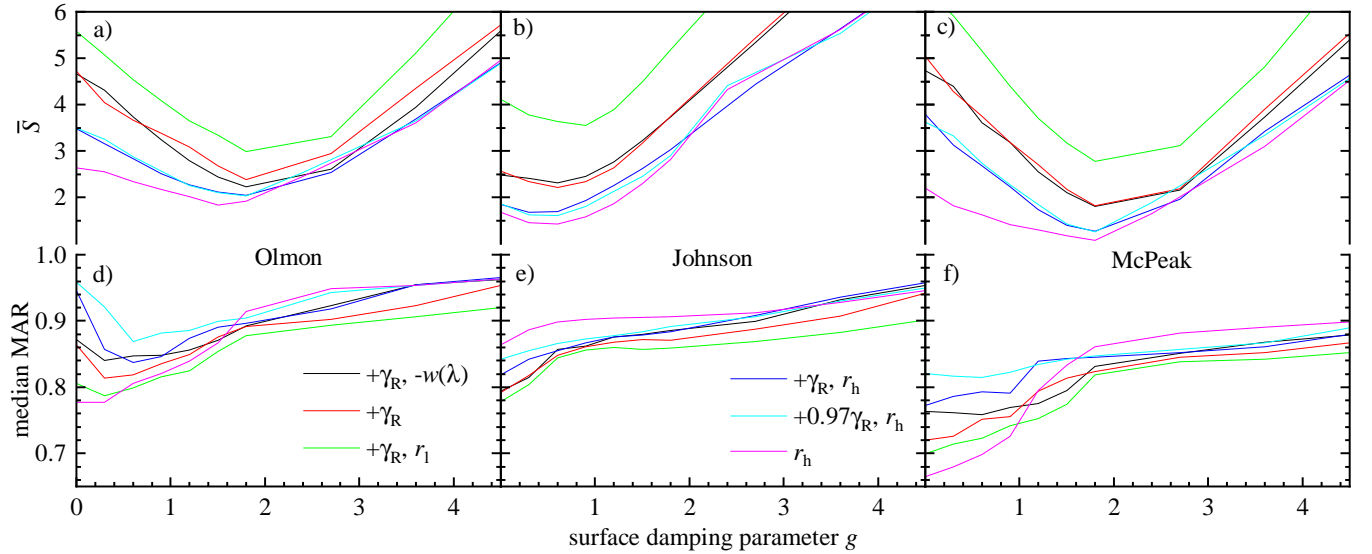


FIG. 12. Median error \bar{S} and median MAR of ON analysis as function of surface damping parameter g , for permittivity datasets as indicated. Results for various analysis settings are shown, labelled as follows: $+\gamma_R$, $+0.97\gamma_R$: inclusion of radially polarised measurements, unscaled or scaled by a factor of 0.97, respectively; $-w(\lambda)$: no correction for the lamp spectrum and camera sensitivity; r_l , r_h : extinction data measured using the integration radius r_l or r_h , respectively.

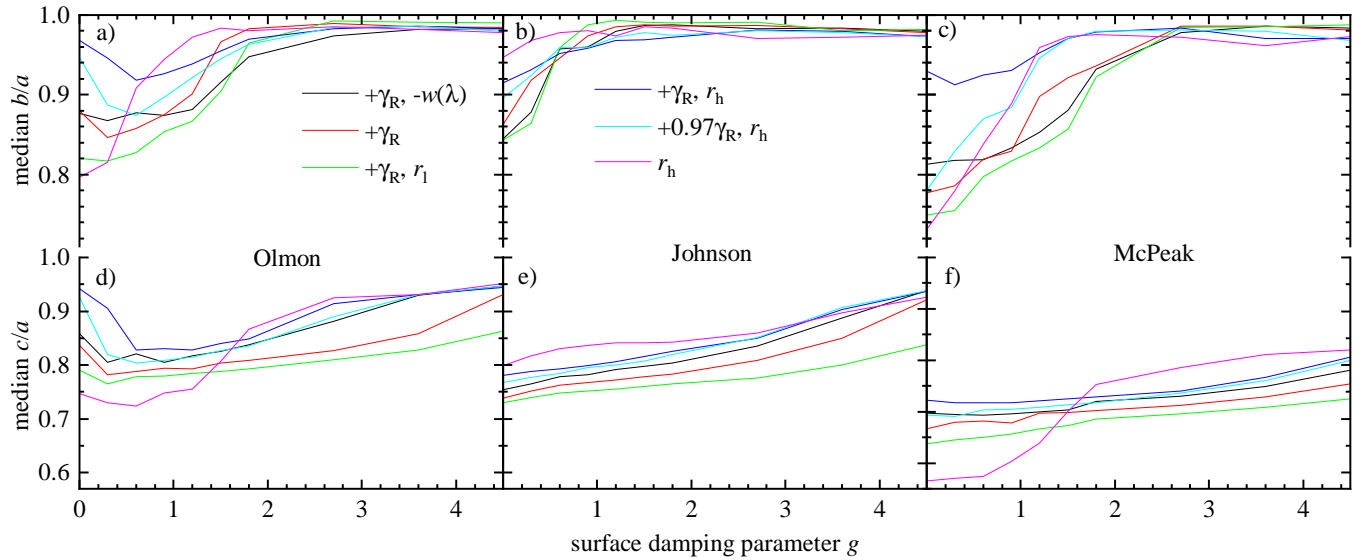


FIG. 13. As Fig. 12, but for the median of b/a and c/a .

nation NA to reduce r_l to the minimum necessary to collect the full extinction, and additionally reduce cross-talk between nearby NPs. Generally one could simply increase s and use a lower sample density. Furthermore, one can improve the focussing procedure or use automated focusing techniques. This work elucidates how the accuracy of extinction measurements within an experiment can affect the spread of retrieved sizes, beyond the photon- and sample-induced measurement noise.

Appendix E: Effect of corrections on retrieved NP morphometry

In Fig. 12 and 13, we explore how the various corrections and minor improvements to the extinction and shape retrieval analyses affects the outcome of the ON. Specifically, we look at the effects of inclusion of lamp spectrum and camera sensitivity, use of different r_l in the extinction analysis, inclusion of $\sigma_{\text{ext}}(\gamma_R)$, and a correction of $\sigma_{\text{ext}}(\gamma_R)$ by a factor 0.97, compensating the difference between $\sigma_{\text{ext}}(\gamma_R)$ and $\sigma_{\text{ext}}(\gamma_P)$ as discussed in the Sec. IV A and observed in Fig. 2. We find (see

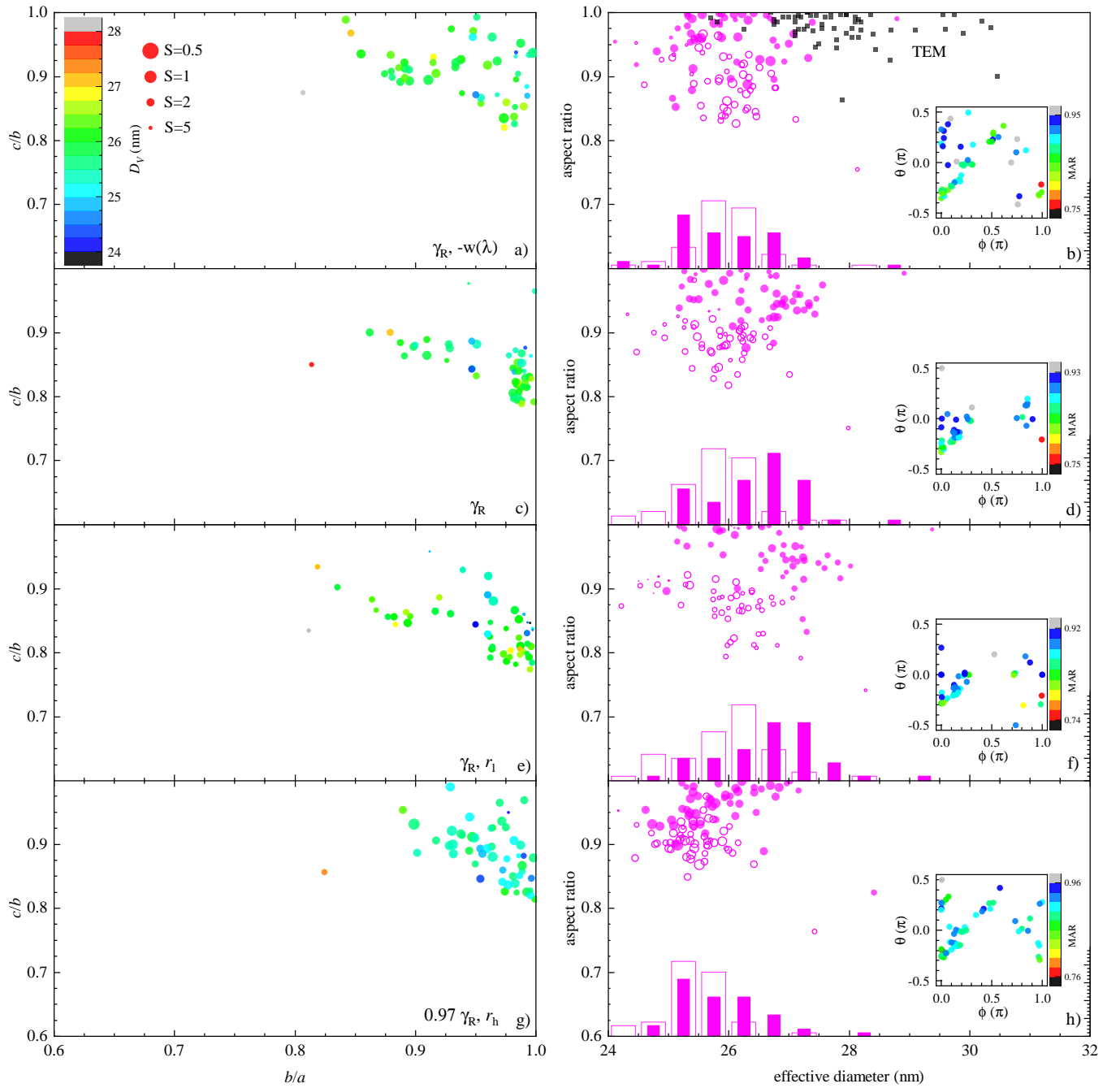


FIG. 14. Morphometric results for $N = 51$ nominally $D = 30\text{nm}$ UGNs, for OL with $g = 1.8$, similar to Fig. 4, but for different analysis settings. Left: fitted aspect ratios c/b versus b/a . The symbol size indicates the error of the fit using $(1 + S)^{-1}$, as given in a), while the colour indicates the volume-equivalent diameter, D_V , as given in a). Right: MAR versus D_V (empty circles) and PAR versus D_p (filled circles), symbol sizes as in a). In b) the TEM data PAR versus D_p for the $N = 51$ UGNs is shown for reference. The histograms of D_V (empty) and D_p (filled) are also shown. The insets show the fitted angles, θ versus ϕ , with a symbol colour indicating the MAR as given in the scale. Using the designations introduced in Fig. 12, panels (a,b) refer to $+\gamma_R, -w(\lambda)$; (c,d) to $+\gamma_R$; (e,f) to $+\gamma_R, r_1$; and (g,h) to $+0.97\gamma_R, r_h$.

Fig. 12a-c) that the dominant effect on \bar{S} are offsets, while the value of g for minimum \bar{S} is less affected. The largest \bar{S} is found using r_1 , as expected from the larger defocussing artefacts. We find that when $\sigma_{\text{ext}}(\gamma_R)$ is not included, \bar{S} reaches its lowest value across all cases, as expected by the reduced constraints on the fit, see also Sec. IV B. Including $\sigma_{\text{ext}}(\gamma_R)$,

the lowest \bar{S} is found using $0.97\sigma_{\text{ext}}(\gamma_R)$, including $w(\lambda)$, and using r_h in the extinction analysis. Across the analysis conditions we find \bar{S} is smallest for McPeak, and largest for Olmon.

In Fig. 12(d-f) and Fig. 13 we show the dependence of the aspect ratios on g for the different permittivity datasets and analysis conditions. A considerably stronger dependence on g

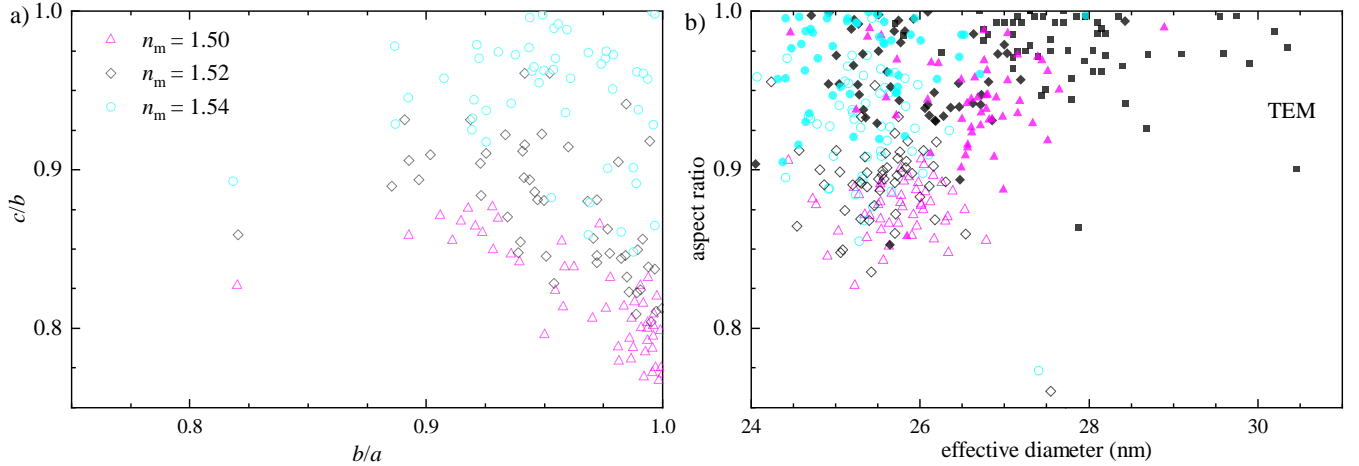


FIG. 15. Morphometric results for $N = 51$ nominally $D = 30$ nm UGNs, for OL with $g = 1.8$ similar to Fig. 4, but for varying medium index n_m . a) fitted aspect ratios c/b versus b/a . b) MAR versus D_V (empty symbols), and PAR versus D_p (filled symbols). The black filled squares indicate TEM measurements PAR versus D_p . Results are shown for the nominal index $n_m = 1.52$ (black diamonds), a lower index $n_m = 1.50$ (magenta triangles), and a higher index $n_m = 1.54$ (cyan circles).

is observed for b/a than for c/a , with b/a obtaining close to its maximal value typically for \bar{S} at its minimum, and plateauing for increasing g . This can be understood by the broadening of the resonance, increasing the cross-sections at wavelengths longer than the LSPR, which otherwise requires non-spherical shapes shifting the LSPR to the red.

We show the distributions of retrieved shapes and sizes for the different analysis conditions in Fig. 14. The condition $+0.97\gamma_R, +r_h$ (panels g,h) provides the smallest spread and the roundest particles, closest to the shape seen in TEM of all conditions apart from those using $\epsilon_{NP}^s(\lambda)$ seen in Sec. IV B and Fig. 5. At the same time, it provides the smallest D_V , about 2 nm lower than TEM. This points towards a systematic error of the model. As discussed in Sec. IV B and Sec. V, the most likely source for this is retardation effects leading to a reduction of the cross-section, broadening by radiative damping, and red-shift compared to the static approximation used in our model.

Appendix F: Effect of medium refractive index on retrieved NP morphometry

The effects of deviations of the refractive index of the NP environment from its nominal value $n_m = 1.52$ on the morphometric retrieval are shown in Fig. 15 for OL with $g = 1.8$, with other analysis conditions as for the results seen in Fig. 4. We use changes of ± 0.02 , which fully cover the range that might be expected from spectral dispersion in glass or silicone oil over the probed wavelength range, or batch-to-batch material variations. We find that the dominant effect is on the retrieved shape, specifically on the AR c/b which changes by about twice the index change. Such a behaviour is expected from the red-shift of the LSPR with increasing n_m , which is compensated by a reduced asymmetry-induced red-shift. These results indicate that the medium refractive index

accuracy needs to be better than half the required aspect ratio accuracy. A slight change of the retrieved size is also seen, by about ∓ 0.25 nm for ± 0.02 index change.

Appendix G: Effect of retardation on retrieved NP morphometry

Here, we consider if the few percent difference in aspect ratio and size between the retrieved morphometries and the TEM-measurements is in part attributable to the fact that the dipole approximation does not take into account retardation effects. Specifically, in Fig. 16, we show the extinction spectra for a spherical NP of 27.94 nm diameter plotted for all g used in the analysis for each of the three permittivity datasets in the main text calculated using the Rayleigh-Gans theory. These are compared with calculations using Mie theory (dotted lines) at $g = 0$ and g yielding the minimum \bar{S} for each of the three permittivity datasets. Importantly, we see that there is a small but noticeable red-shift in the peak of spectra calculated using Mie theory which includes retardation. Such a redshift can in the Rayleigh-Gans theory only be achieved by increasing the shape asymmetry. To account for the red-shift from retardation without introducing a new model into the analysis, we shift the permittivity data by $\delta\lambda \in \{-4, -6, -8, -10\}$ nm, introducing $\epsilon_{NP}^s(\lambda) = \epsilon_{NP}(\lambda + \delta\lambda)$. We then perform the ON analysis using ϵ_{NP}^s . To ensure we are not limited by the discussed small discrepancy between the linear and radial measurements of σ_{ext} , we performed this additional analysis using the $0.97\times$ correction to the $\sigma_{ext}(\gamma_R)$ data.

We examine the resulting dependence of \bar{S} and the median MAR and PAR on g for the different $\delta\lambda$ in Fig. 17. The JC permittivity is the only one where \bar{S} does not decrease for some $\delta\lambda < 0$. Meanwhile, OL and MP both show a minimum of \bar{S} for $\delta\lambda = -4$ nm, before the error begins increasing past the original $\delta\lambda = 0$ case. MP shows a less clear dependence

of MAR on g for the different $\delta\lambda$ compared to OL, but in all permittivities, increased $\delta\lambda$ shows increased average roundness of the retrieved morphometries.

¹X. Han, K. Xu, O. Taratula, and K. Farsade, "Applications of nanoparticles in biomedical imaging," *Nanoscale* **11**, 799–819 (2019).

²I. Pope, H. Tanner, F. Masia, L. Payne, K. P. Arkill, J. Mantell, W. Langbein,

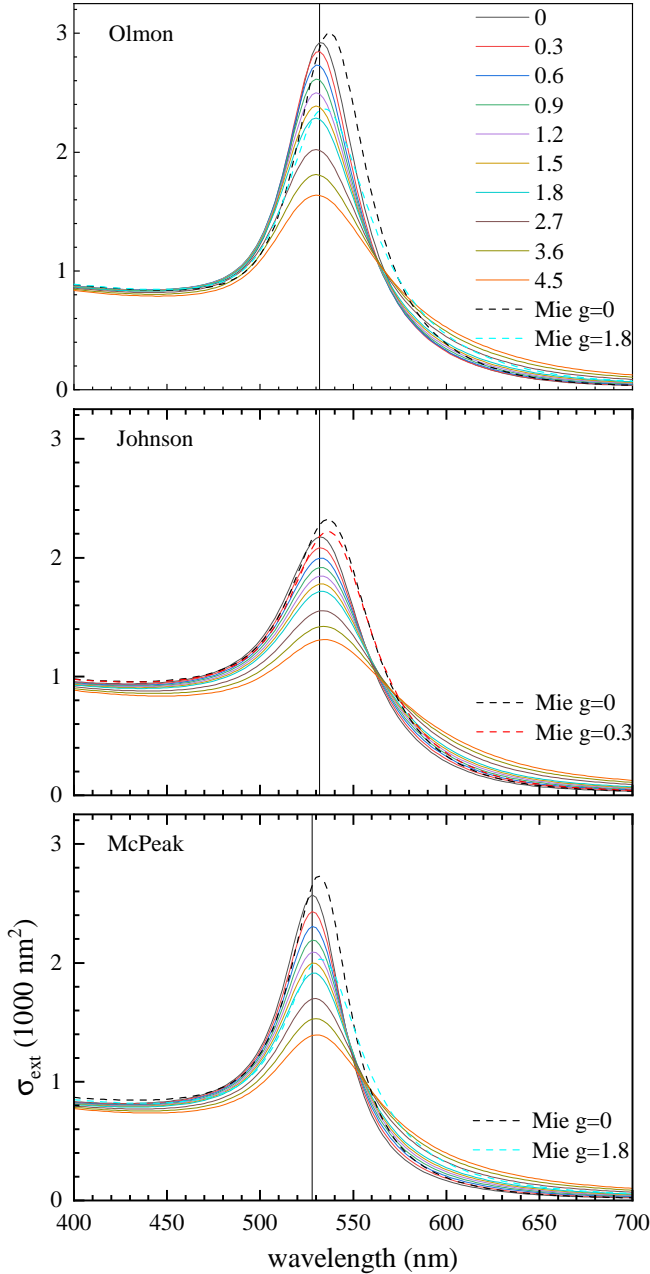


FIG. 16. Solid curves : $\sigma_{\text{ext}}(\lambda)$ for a spherical NP of 27.94 nm diameter calculated for a range of g as indicated and each of the three permittivity datasets described in the main text using the Rayleigh-Gans theory. Dotted curves : as above, but calculated using Mie theory at $g = 0$ and the g at which minimum \bar{S} was obtained in the morphometric retrieval for each of the three permittivities ($g = (1.8, 0.3, 1.8)$ for OL, JC, and MP, respectively). Vertical lines indicate the peak position in $\sigma_{\text{ext}}(\lambda)$ for $g = 0$ for the Rayleigh-Gans theory.

P. Borri, and P. Verkade, "Correlative light-electron microscopy using small gold nanoparticles as single probes," *Light Sci Appl* **12**, 80 (2023).

³J. Kneipp, "Interrogating cells, tissues, and live animals with new generations of surface-enhanced raman scattering probes and labels," *ACS Nano* **11**, 1136–1141 (2017).

⁴R. M. Pallares, N. T. K. Thanh, and X. Su, "Sensing of circulating cancer biomarkers with metal nanoparticles," *Nanoscale* **11**, 22152–22171 (2019).

⁵H. Atwater and A. Polman, "Plasmonics for improved photovoltaic devices," *Nat. Mater.* **9**, 205–213 (2010).

⁶G. J. Hutchings, "Heterogeneous gold catalysis," *ACS Cent. Sci.* **4**, 1095–1101 (2018).

⁷T. Sun, Y. S. Zhang, B. Pang, D. C. Hyun, M. Yang, and Y. Xia, "Engineered nanoparticles for drug delivery in cancer therapy," *Angew. Chem. Int. Ed.* **53**, 12320–12364 (2014).

⁸P. Liu, G. Chen, and J. Zhang, "A review of liposomes as a drug delivery system: Current status of approved products, regulatory environments, and future perspectives," *Molecules* **27** (2022), 10.3390/molecules27041372.

⁹N. B. Turan, G. O. Engin, and M. S. Bilgili, "Chapter nine - nanoparticles in solid waste: Impact and management strategies," in *Environmental Nanotechnology: Implications and Applications*, Comprehensive Analytical Chemistry, Vol. 99, edited by N. B. Turan, G. O. Engin, and M. S. Bilgili (Elsevier, 2022) pp. 241–260.

¹⁰S. Chaturvedi, D. Maheshwari, A. Chawathe, and N. Sharma, "Current analytical approaches for characterizing nanoparticle sizes in pharmaceutical research," *J. Nanopart. Res.* **26** (2024), 10.1007/s11051-023-05924-x.

¹¹W. D. Pyrz and D. J. Buttrey, "Particle size determination using tem: A discussion of image acquisition and analysis for the novice microscopist," *Langmuir* **24**, 11350–11360 (2008).

¹²L. Calzolari, D. Gilliland, and F. Rossi, "Measuring nanoparticles size distribution in food and consumer products: a review," *Food Additives & Contaminants: Part A* **29**, 1183–1193 (2012).

¹³F. Caputo, J. Clogston, L. Calzolari, M. Rösslein, and A. Prina-Mello, "Measuring particle size distribution of nanoparticle enabled medicinal products, the joint view of euclid and nci-ncl. a step by step approach combining orthogonal measurements with increasing complexity," *J. Controlled Release* **299**, 31–43 (2019).

¹⁴S. Gioria, F. Caputo, P. Urbán, C. M. Maguire, S. Bremer-Hoffmann, A. Prina-Mello, L. Calzolari, and D. Mehn, "Are existing standard methods suitable for the evaluation of nanomedicines: some case studies,"

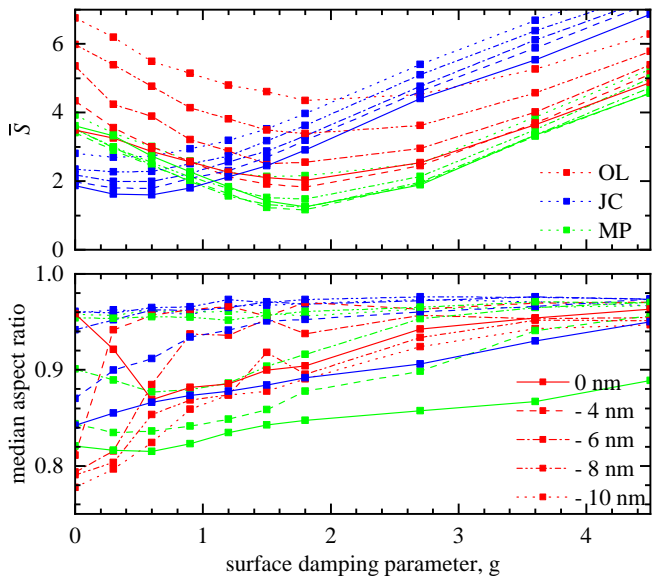


FIG. 17. \bar{S} and median MAR for $N = 51$ UGNS of nominal $D = 30$ nm for varying surface damping parameter g as in Fig. 3, but using $\epsilon_{\text{NP}}^s(\lambda)$ for different ϵ_{NP} datasets indicated by color and wavelength shifts $\delta\lambda$ indicated by line type, as labelled.

- Nanomedicine **13**, 539–554 (2018).
- ¹⁵M. Wagner, S. Holzschuh, A. Traeger, A. Fahr, and U. Schubert, “Asymmetric flow field-flow fractionation in the field of nanomedicine,” *Anal. Chem.* **86**, 5201–5210 (2014).
- ¹⁶R. Vogel, G. Wilmott, D. Kozak, G. S. Roberts, W. Anderson, L. Groenewegen, B. Glossop, A. Barnett, A. Turner, and M. Trau, “Quantitative sizing of nano/microparticles with a tunable elastomeric pore sensor,” *Anal. Chem.* **83**, 3499–3506 (2011).
- ¹⁷R. R. Henriquez, T. Ito, L. Sun, and R. M. Crooks, “The resurgence of coulter counting for analyzing nanoscale objects,” *Analyst* **129**, 478–482 (2004).
- ¹⁸B. J. Berne and R. Pecora, “Dynamic light scattering: With applications to chemistry, biology, and physics,” (1976).
- ¹⁹N. C. Bell, C. Minelli, J. Tompkins, M. M. Stevens, and A. G. Shard, “Emerging techniques for submicrometer particle sizing applied to stöber silica,” *Langmuir* **28**, 10860–10872 (2012).
- ²⁰K. S. Sillmore, X. Gong, M. S. Strano, and J. W. Swan, “High-resolution nanoparticle sizing with maximum a posteriori nanoparticle tracking analysis,” *ACS Nano* **13**, 3940–3952 (2019).
- ²¹A. D. Kashkanova, M. Blessing, A. Gemeinhardt, D. Soulat, and V. Sandoghdar, “Precision size and refractive index analysis of weakly scattering nanoparticles in polydispersions,” *Nat. Methods* **19**, 586–593 (2022).
- ²²B. Špačková, H. Klein Moberg, J. Fritzsche, J. Tenghamn, G. Sjösten, H. Šípová Jungová, D. Albinsson, Q. Lubart, D. van Leeuwen, F. Westerlund, D. Midtvedt, E. K. Esbjörner, M. Käll, G. Volpe, and C. Langhammer, “Label-free nanofluidic scattering microscopy of size and mass of single diffusing molecules and nanoparticles,” *Nat. Methods* **19**, 751–758 (2022).
- ²³J. G. Walker, P. C. Y. Chang, K. I. Hopcraft, and E. Mozaffari, “Independent particle size and shape estimation from polarization fluctuation spectroscopy,” *Meas. Sci. Technol.* **15**, 771 (2004).
- ²⁴S. Dawda, Z. Shen, and A. Dogariu, “Measuring nanoparticles shape by structured illumination,” *Sci. Rep.* **14** (2024), 10.1038/s41598-024-53665-1.
- ²⁵R. Attota, P. P. Kavuri, H. Kang, R. Kasica, and L. Chen, “Nanoparticle size determination using optical microscopes,” *Appl. Phys. Lett.* **105**, 163105 (2014), https://pubs.aip.org/aip/apl/article-pdf/doi/10.1063/1.4900484/14025666/163105_1_online.pdf.
- ²⁶O. Avci, C. Yurdakul, and M. S. Ünlü, “Nanoparticle classification in wide-field interferometric microscopy by supervised learning from model,” *Appl. Opt.* **56**, 4238–4242 (2017).
- ²⁷J. T. Trueb, O. Avci, D. Sevenler, J. H. Connor, and M. S. Ünlü, “Robust visualization and discrimination of nanoparticles by interferometric imaging,” *IEEE J. Sel. Topics Quantum Electron.* **23**, 394–403 (2017).
- ²⁸S. Khadir, D. Andrén, P. C. Chaumet, S. Monneret, N. Bonod, M. Käll, A. Sentenac, and G. Baffou, “Full optical characterization of single nanoparticles using quantitative phase imaging,” *Optica* **7**, 243–248 (2020).
- ²⁹C. Gentner, B. Rogez, H. M. L. Robert, A. Aggoun, G. Tessier, P. Bon, and P. Berto, “Enhanced quantitative wavefront imaging for nano-object characterization,” *ACS Nano* **18**, 19247–19256 (2024).
- ³⁰D. Boyer, P. Tamarat, A. Maali, B. Lounis, and M. Orrit, “Photothermal imaging of nanometer-sized metal particles among scatterers,” *Science* **297**, 1160–1163 (2002).
- ³¹M. Husnik, S. Linden, R. Diehl, J. Niegemann, K. Busch, and M. Wegener, “Quantitative experimental determination of scattering and absorption cross-section spectra of individual optical metallic nanoantennas,” *Phys. Rev. Lett.* **109**, 233902 (2012).
- ³²A. Tcherniak, J. W. Ha, S. Dominguez-Medina, L. S. Slaughter, and S. Link, “Probing a century old prediction one plasmonic particle at a time,” *Nano Lett.* **10**, 1398–1404 (2010).
- ³³A. Crut, P. Maioli, N. D. Fatti, and F. Vallée, “Optical absorption and scattering spectroscopies of single nano-objects,” *Chem. Soc. Rev.* **43**, 3921–3956 (2014).
- ³⁴L. M. Payne, W. Langbein, and P. Borri, “Polarization-resolved extinction and scattering cross-section of individual gold nanoparticles measured by wide-field microscopy on a large ensemble,” *Appl. Phys. Lett.* **102**, 131107 (2013).
- ³⁵A. Zilli, W. Langbein, and P. Borri, “Quantitative measurement of the optical cross sections of single nano-objects by correlative transmission and scattering microspectroscopy,” *ACS Photonics* **6**, 2149–2160 (2019).
- ³⁶A. Arbouet, D. Christofilos, N. Del Fatti, F. Vallée, J. R. Huntzinger, L. Arnaud, P. Billaud, and M. Broyer, “Direct measurement of the single-metal-cluster optical absorption,” *Phys. Rev. Lett.* **93**, 127401 (2004).
- ³⁷O. L. Muskens, P. Billaud, M. Broyer, N. Del Fatti, and F. Vallée, “Optical extinction spectrum of a single metal nanoparticle: Quantitative characterization of a particle and of its local environment,” *Phys. Rev. B* **78**, 205410 (2008).
- ³⁸G. Mie, “Beiträge zur Optik trüber Medien, speziell kolloidaler Metallösungen,” *Ann. Phys.* **330**, 377–445 (1908).
- ³⁹C. F. Bohren and D. R. Huffman, *Absorption and scattering of light by small particles* (John Wiley & Sons, New York, 1983).
- ⁴⁰S. V. Lobanov, W. Langbein, and E. A. Muljarov, “Resonant-state expansion of three-dimensional open optical systems: Light scattering,” *Phys. Rev. A* **98**, 033820 (2018).
- ⁴¹Y. Wang, A. Zilli, Z. Sztranyovszky, W. Langbein, and P. Borri, “Quantitative optical microspectroscopy, electron microscopy, and modelling of individual silver nanocubes reveals surface compositional changes at the nanoscale,” *Nanoscale Adv.* **2**, 2485–2496 (2020).
- ⁴²Y. Wang, Z. Sztranyovszky, A. Zilli, W. Albrecht, S. Bals, P. Borri, and W. Langbein, “Quantitatively linking morphology and optical response of individual silver nanohedra,” *Nanoscale* **14**, 11028–11037 (2022).
- ⁴³L. M. Payne, W. Albrecht, W. Langbein, and P. Borri, “The optical nanosizer – quantitative size and shape analysis of individual nanoparticles by high-throughput widefield extinction microscopy,” *Nanoscale* **12**, 16215–16228 (2020).
- ⁴⁴L. M. Payne, F. Masia, A. Zilli, W. Albrecht, P. Borri, and W. Langbein, “Quantitative morphometric analysis of single gold nanoparticles by optical extinction microscopy: Material permittivity and surface damping effects,” *J. Chem. Phys.* **154**, 044702 (2021), https://pubs.aip.org/aip/jcp/article-pdf/doi/10.1063/5.0031012/13945732/044702_1_online.pdf.
- ⁴⁵P. B. Johnson and R. W. Christy, “Optical constants of noble metals,” *Phys. Rev. B* **6**, 4370–4379 (1972).
- ⁴⁶K. M. McPeak, S. V. Jayanti, S. J. P. Kress, S. Meyer, S. Iotti, A. Rossinelli, and D. J. Norris, “Plasmonic films can easily be better: Rules and recipes,” *ACS Photon.* **2**, 326–333 (2015).
- ⁴⁷R. L. Olmon, B. Slovick, T. W. Johnson, D. Shelton, S.-H. Oh, G. D. Boreman, and M. B. Raschke, “Optical dielectric function of gold,” *Phys. Rev. B* **86**, 235147 (2012).
- ⁴⁸F. Masia, W. Langbein, and P. Borri, “Measurement of the dynamics of plasmons inside individual gold nanoparticles using a femtosecond phase-resolved microscope,” *Phys. Rev. B* **85**, 235403 (2012).
- ⁴⁹M. Guerrisi, R. Rosei, and P. Winsemius, “Splitting of the interband absorption edge in Au,” *Phys. Rev. B* **12**, 557–563 (1975).
- ⁵⁰C. Voisin, D. Christofilos, P. A. Loukakos, N. D. Fatti, F. Vallée, J. Lermé, M. Gaudry, E. Cottancin, M. Pellarin, and M. Broyer, “Ultrafast electron-electron scattering and energy exchanges in noble-metal nanoparticles,” *Phys. Rev. B* **69**, 195416 (2004).
- ⁵¹D. Gall, “Electron mean free path in elemental metals,” *J. Appl. Phys.* **119**, 085101 (2016).
- ⁵²F. Alabdullah, V. Singh, L. Payne, D. Regan, F. Masia, V. G. Rocha, W. Langbein, and P. Borri, “Radially polarized light in single particle optical extinction microscopy identifies silver nanoplates,” *Appl. Phys. Lett.* **124**, 181105 (2024).
- ⁵³L. M. Payne, W. Langbein, and P. Borri, “Wide-field imaging of single-nanoparticle extinction with sub-nm² sensitivity,” *Phys. Rev. Appl.* **9**, 034006 (2018).
- ⁵⁴L. Payne, *Optical extinction and coherent multiphoton micro-spectroscopy of single nanoparticles*, Ph.D. thesis, Cardiff University (2016).
- ⁵⁵L. Payne, A. Zilli, Y. Wang, W. Langbein, and P. Borri, “Quantitative high-throughput optical sizing of individual colloidal nanoparticles by wide-field imaging extinction microscopy,” in *Proc. SPIE 10892, Colloidal Nanoparticles for Biomedical Applications XIV*, Vol. 10892 (2019) pp. Colloidal Nanoparticles for Biomedical Applications XIV, 108920J.
- ⁵⁶T. Christensen, W. Yan, A.-P. Jauho, M. Soljačić, and N. A. Mortensen, “Quantum corrections in nanoplasmonics: Shape, scale, and material,” *Phys. Rev. Lett.* **118**, 157402 (2017).
- ⁵⁷R. Hartley and A. Zisserman, *Multiple view geometry in computer vision* (Cambridge university press, 2003).
- ⁵⁸R. J. Yamartino, “A Comparison of Several ‘Single-Pass’ Estimators of the Standard Deviation of Wind Direction,” *J. Clim. Appl. Meteorol.* **23**, 1362–1366 (1984).